



# Hydrological drivers of hydrogen cyanide wildfire emissions from Indonesian peat fires during the 2015, 2019, and 2023 El Niño events

Antonio G. Bruno<sup>1,2</sup>, David P. Moore<sup>1,2</sup>, Jeremy J. Harrison<sup>1,2</sup>, Ailish Graham<sup>3,4</sup>, and Martyn P. Chipperfield<sup>3,4</sup>

Correspondence: A. G. Bruno (agb22@leicester.ac.uk)

**Abstract.** Indonesian peatlands store vast amounts of carbon that are highly vulnerable to fire during El Niño-driven droughts. When ignited, peats release large quantities of greenhouse gases and other species with significant environmental impacts, including hydrogen cyanide (HCN), a sensitive tracer of smouldering combustion. In this work, we use satellite retrievals from the Infrared Atmospheric Sounding Interferometer (IASI), TOMCAT atmospheric model simulations, hydrological information, and fire activity observations to evaluate the factors driving trace gas emissions during the 2015, 2019, and 2023 El Niño events

The 2015 El Niño produced large burdens of HCN and CO unprecedented in the satellite observational era, driven by exceptionally low soil moisture, depressed groundwater levels, and deep burn depths. In contrast, the 2019 and 2023 events exhibited markedly weaker emissions despite similar Oceanic Niño Index (ONI) anomalies, reflecting more favourable hydrological conditions. Comparisons of the satellite trace gas observations with simulations of the TOMCAT model show that burned-area-based inventories such as GFED substantially overestimate emissions from peat fires in 2015, while a new peat-specific database, FINNpeatSM, better represents fire season timing and burn depth by incorporating soil moisture constraints. From satellite-derived HCN:CO enhancement ratios, we provide new emission factors for HCN that offer benchmarks for new emission inventories.

Our results show that peat fire intensity and emissions are driven not only by El Niño strength but also by local hydrological conditions such as soil water content and precipitation. Integrating hydrological indicators with satellite observations of atmospheric composition is therefore critical for improving fire emission inventories.

## 1 Introduction

During the South-East Asian dry season, El Niño generally has a strong influence on the conditions driving widespread fires. Fires are commonly used across the region for land clearing to manage fields and prepare the soil for the growing season. However, much of the land in Kalimantan and Sumatra, Indonesia, is underlain by tropical peat soils that have been extensively drained using a network of canals. Dry conditions and elevated temperatures, typical of the dry season, are particularly exac-

<sup>&</sup>lt;sup>1</sup>School of Physics and Astronomy, University of Leicester, Leicester, UK

<sup>&</sup>lt;sup>2</sup>National Centre for Earth Observation, University of Leicester, Leicester, UK

<sup>&</sup>lt;sup>3</sup>School of Earth and Environment, University of Leeds, Leeds, UK

<sup>&</sup>lt;sup>4</sup>National Centre for Earth Observation, University of Leeds, Leeds, UK





erbated in the Indonesian environment during El Niño, making man-made fires more difficult to control (Parker et al., 2016). Under these conditions, vegetation fires can ignite the underlying carbon-rich peat soils, causing wildfires that are extremely difficult to extinguish and that can burn for weeks.

Indonesian peatlands occupy about 55% of the tropical peatland carbon reservoir (Dargie et al., 2017; Page and Hooijer, 2016). They store extremely large amounts of partially decayed organic matter, and release substantial amounts of pyrogenic trace gas species and particulate matter into the atmosphere when burned. The carbon stored can be emitted in the form of trace gases such as carbon dioxide (CO<sub>2</sub>), carbon monoxide (CO) and hydrogen cyanide (HCN), the latter also badly affecting the air quality across South-East Asia. In particular, during El Niño years strong peaks in global HCN have been observed (Park et al., 2021; Rosanka et al., 2021), suggesting that it is a good atmospheric tracer for peat fire (Pumphrey et al., 2018; Sheese et al., 2017). Monitoring HCN emissions is therefore important in understanding severe peatland fires, and for understanding global carbon accounting.

Peatlands are particularly vulnerable to smouldering fires, which are characterised by slow, low-temperature, flameless combustion. Peat fires typically develop in three stages (Usup et al., 2004). In the first, surface peat is ignited due to a surface fire event. In the second stage a smouldering front burns laterally and downward into the surface (up to 20 cm), and in the third the smouldering extends into deeper peat layers below 20 cm in depth. It is the latter smouldering stages in which HCN is primarily released. Ultimately, it is the peat soil moisture, in particular the ground water level (GWL), that determines the ignition and spread of these smouldering fires.

During the period September to November 2015, under the influence of a strong El Niño, Indonesia experienced the most severe wildfire season of the last three decades. The intensity of the 2015-2016 El Niño event (ONI: +2.6 deg C) was comparable to the 1997-1998 El Niño (ONI: +2.4 deg C)(Anthony G. Bamston and Goldenberg, 1997; Huang et al., 2017), one of the strongest recorded (Field et al., 2016; Santoso et al., 2017). The peatland fires lasted for about three months during which more than 2.6 Mha of forest, peat and other land types were burned, and an equivalent of 5% of the global 2015 fossil fuel CO<sub>2</sub> emissions were released (Vetrita and Cochrane, 2020). In the period 1997-2016, fires in equatorial Asia and particularly Indonesia produced about 8% of the global fire carbon emissions (van der Werf et al., 2017).

The 2023-2024 El Niño period is currently the second strongest event of this century (ONI: 2.0 deg C), falling just behind that of 2015-2016. However, as will be shown, there is a marked difference in the behaviour of the fire plumes and the amount of HCN released. While previous studies have documented the role of El Niño in intensifying Indonesian fire activity (Field et al., 2016; Whitburn et al., 2017; Nurdiati et al., 2021), large uncertainties remain in quantifying trace gas emissions from peatland combustion, particularly for hydrogen cyanide (HCN), a key tracer of peat fires. Existing fire inventories, such as Global Fire Emissions Database (GFED), rely heavily on burned-area estimates that are poorly suited to capturing underground peat burning and thus tend to misrepresent both the timing and magnitude of emissions. In this paper, we systematically compare multiple El Niño events to evaluate the influence of large-scale climate forcing and local hydrological parameters on peat fire dynamics. We provide new satellite-based constraints on HCN emission factors, evaluate the performance of the GFED emission inventory, introduce a new database based on the method developed for FINNpeatSM (Kiely et al., 2019), and assess how variations in soil moisture and groundwater level influence interannual differences in wildfire dynamics and emissions.





The paper is structured as follows. Section 2 describes the main datasets and models used in this study. In Section 3.1, we investigate HCN emissions during the 2015 Indonesian fire season using total columns retrieved from the University of Leicester IASI Retrieval Scheme (ULIRS) (Moore et al., in Preparation), and compare with recent TOMCAT model simulations (Bruno et al., 2022, 2023). In this section, we also propose a new estimate of HCN emission factors by calculating the enhancement ratio between HCN and CO,  $ER_{HCN/CO}$ . Section 3.2 discusses the differences between the 2015, 2019, and 2023 fire seasons and explores their underlying causes, focusing on soil moisture and precipitation as the principal hydrological drivers of fire activity, using the FINNpeatSM approach (Kiely et al., 2019). Finally, Section 4 synthesizes the main findings of this work and highlights the implications of hydrological controls for peatland fire dynamics and trace gas emissions.

#### 2 Data

## 2.1 Atmospheric CO and HCN data

#### 2.1.1 IASI

IASI is a hyperspectral sounder onboard the three polar-orbiting MetOp satellites, launched in 2006 (IASI-A, now decommissioned), 2012 (IASI-B), and 2018 (IASI-C) jointly by CNES (Centre National d'Études Spatiales, French agency) and EU-METSAT (European Organisation for the Exploitation of Meteorological Satellites). The main objective of IASI is to provide a continuous and long-term collection of measurements to support meteorology, namely temperature and humidity tropospheric profiles with high vertical resolution and precision, but it has also been used to monitor both the environment and climate on a global scale through observations of atmospheric composition (Clerbaux et al., 2009; Hilton et al., 2012).

IASI measures the spectrally resolved thermal infrared radiation emitted by the Earth and the atmosphere system at the top of the atmosphere (TOA). Due to its high spectral resolution and spectral sampling, IASI is able to measure a large number of trace gases, including some species observed only sporadically in the measured spectra (Clerbaux et al., 2009; Clarisse et al., 2011). These species include 10 gases with clear spectral signatures that are always present in the satellite measurements, CO<sub>2</sub>, N<sub>2</sub>O, CFC-11, CFC-12, OCS, H<sub>2</sub>O, CH<sub>4</sub>, O<sub>3</sub>, CO and HNO<sub>3</sub> (Clarisse et al., 2011; Clerbaux et al., 2009) and 14 reactive trace gases. Some of these reactive gases are the typical products of biomass burning, such as HCN, which has been assessed in previous IASI studies, and is retrieved using the absorption band centered at 712 cm<sup>-1</sup> (ν<sub>2</sub> band) (Coheur et al., 2009; De Longueville et al., 2021; Duflot et al., 2015, 2013).

The sensitivity of IASI retrievals near the surface is limited and exhibits a strong dependence on thermal contrast (with large differences between daytime and nighttime), which constrains the amount of vertical information that can be obtained. For CO, the averaging kernels indicate two distinct vertical contributions: one from the lower troposphere, peaking on average at about 5 km, and another from the upper troposphere, near 10 km. In contrast, HCN retrievals are primarily sensitive to the mid to upper troposphere, with peak sensitivity between 9 and 12 km. The concentrations of HCN and CO during the 2015, 2019 and 2023 fire seasons were retrieved using the University of Leicester IASI Retrieval Scheme (ULIRS). A comprehensive description of the retrieval methodology for both CO and HCN, along with their validation, is provided in Moore et al. (in





Preparation). In essence, the ULIRS retrieves atmospheric trace gas partial and total column information from IASI top-of-atmosphere radiances. To do this, the scheme incorporates an optimal estimation method (Rodgers, 2000) to constrain the inversion with a priori information about the variables to be retrieved, in this case HCN, alongside H<sub>2</sub>O, CO<sub>2</sub> and temperature (profile and surface). For CO, a single global average a priori profile was constructed with ACE v3.6 data (Bernath et al., 2021) covering 2004 to 2018 for the stratospheric profile and one-sigma uncertainty (above 15 km) and merged with the troposphere (below 15 km) using TOMCAT model data over the 2006 to 2015 period. For HCN, the a priori profile was constructed from INTEX-B aircraft information (Singh et al., 2009) in the troposphere and ACE v4 data (Boone et al., 2020) in the stratosphere over polluted scenes. A loose constraint on the HCN a priori uncertainty of 300% was assumed.

#### **2.1.2 TOMCAT**

105

The TOMCAT 3-D chemical transport model (CTM) is a global offline Eulerian model widely used for both tropospheric and stratospheric chemistry studies. Originally developed as two separate models TOMCAT and SLIMCAT (Chipperfield et al., 1993), the unified model (Chipperfield, 2006; Monks et al., 2017) has since been applied in numerous studies (Chipperfield et al., 2018; Pope et al., 2020; Bruno et al., 2022). The model's meteorological forcings — humidity, temperature, and wind fields — are driven by ERA-Interim reanalysis data from the European Centre for Medium-Range Weather Forecasts (ECMWF), provided at a 6-hour temporal resolution (Berrisford et al., 2011; Dee et al., 2011). These meteorological variables are linearly interpolated to match the temporal resolution and spatial grid of the model. Surface emissions from both natural and anthropogenic sources are incorporated at their original resolution and subsequently re-gridded to align with the model's spatial configuration. Hydrogen cyanide (HCN) emissions are derived from several key datasets: anthropogenic and oceanic emissions are sourced from the Coupled Model Intercomparison Project Phase 6 (CMIP6) (Eyring et al., 2016); biogenic emissions are taken from a fixed annual dataset provided by the Chemistry-Climate Model Initiative (CCMI) (Morgenstern et al., 2017); and biomass burning emissions are obtained from the Global Fire Emissions Database Version 4 (GFED4) (Randerson et al., 2017). A complete description of the tracer version of TOMCAT adapted to simulate global atmospheric HCN distributions has been extensively described in Bruno et al. (2022) and Bruno et al. (2023), and evaluated against independent measurements from ACE-FTS. In this work, we compare TOMCAT outputs with IASI observations.

# 2.2 Precipitation data

115 The Integrated Multi-satellitE Retrievals for GPM (IMERG) is a NASA precipitation product developed under the joint NASA–JAXA Global Precipitation Measurement (GPM) satellite mission. It provides global surface precipitation estimates at 0.1° spatial and 30-minute temporal resolution from June 2000 onward, using data from a constellation of passive microwave sensors, intercalibrated against data from the Tropical Rainfall Measuring Mission (TRMM; 2000–2014) and the GPM Core Observatory (2014–present). IMERG data covers the majority of the Earth's surface and supports a range of applications through three latency products: Early (~4 h), Late (~14 h), and Final (~4 months) (Pradhan et al., 2022).





This study uses the IMERG Final Run daily product (Huffman et al., 2024), derived by averaging valid half-hourly rates and scaling to 24 hours, which reduces the dry biases present in earlier versions. In particular, the data used here cover the period 2014-2023 over Indonesia.

## 2.3 Soil moisture data

#### 125 2.3.1 SMAP

130

The Soil Moisture Active Passive (SMAP) mission, launched by NASA in 2015, is designed to provide global measurements of surface soil moisture and freeze-thaw conditions every 2–3 days (Entekhabi et al., 2014). While the radar instrument ceased operation shortly after launch, the radiometer continues to function reliably, enabling the generation of global soil moisture maps. SMAP data support a better understanding of the Earth's water, energy, and carbon cycles by quantifying the amount of liquid water in the topsoil layer and distinguishing between frozen and unfrozen ground. These observations are essential for improving weather forecasting, climate modeling, and environmental monitoring by capturing temporal changes in soil moisture that influence land-atmosphere interactions and broader ecological processes.

Recent studies have further expanded the scientific utility of SMAP data. Nayak et al. (2025) demonstrated that SMAP-derived surface soil moisture variability is a reliable predictor of subsurface water dynamics. Fang et al. (2024) validated downscaled SMAP products at 1-km resolution using long-term in situ data, confirming their accuracy across heterogeneous landscapes. Additionally, Cho et al. (2024) improved SMAP's performance in dense vegetation regions by calibrating retrieval algorithms to reduce bias. Ma et al. (2024) also enhanced SMAP's global utility by integrating the data with ASCAT observations through machine learning techniques, resulting in higher resolution and more temporally consistent soil moisture estimates.

#### 140 **2.3.2** SWI

The operational SWI is produced by the Copernicus Land Service from the surface soil moisture (SSM) measured by the ASCAT scatterometer onboard the MetOp satellites and from Sentinel-1 C-band SAR. The SWI quantifies from these observations the moisture content of the soil with a spatial resolution of  $0.1^{\circ}$ . It is a dimensionless index ranging from 0 (dry) to 1 (saturated relative to local climatology), at eight different depths as a function of the characteristic timelength T (1, 5, 10, 15, 20, 40, 60 and 100 days), a parameter expressed in units of time but proportional to the depth of the layer, as described in Bauer-Marschallinger et al. (2018).

Differently from other products such as SMAP, the SWI is more an indicator of the percentage of relative wetness than an absolute soil water content, and it is not limited only to the surface soil moisture being able to evaluate water availability at depths typical of the plant roots.





#### 150 2.4 Fire data

155

160

165

#### 2.4.1 GFED emission database

The Global Fire Emissions Database version 4 (GFED4) quantifies biomass burning emissions by coupling satellite-derived burned area (MODIS), active fire detections, and biogeochemical models (van der Werf et al., 2017). The GFED framework estimates dry matter (DM) consumption as a function of fuel load, combustion completeness, and fire activity across different biomes on a monthly  $0.25^{\circ}$  global grid. The trace gas emissions are derived by applying biome-specific emission factors derived from field and lab measurements to the DM consumption (Akagi et al., 2011). The spatial distribution of the DM burned is then determined by using satellite observations of BA in combination with biogeochemical modelling. Cloud cover and a limited knowledge of the biome distribution and emission factors over Indonesia and other peat-dominated regions can cause frequent errors in estimating fire emissions. Another limitation of the approach used to define GFED is its dependence on information about peat consumption by fires — such as the rate, extent, and depth of peat burned — which cannot be easily determined from satellite data (Bruno, 2024).

## 2.4.2 FINNpeatSM emission database

FINNpeatSM (Fire Inventory from NCAR (FINNv1.5) New peat with Soil Moisture) (Kiely et al., 2019) is a bespoke regional dataset for peat fire emissions in Indonesia. FINNpeatSM uses Fire Inventory from NCAR (FINNv1.5) (Wiedinmyer et al., 2011) for fire detections of above ground vegetation fires. FINNv1.5 combines active fire detections from the Moderate Resolution Imaging Spectroradiometer (MODIS), biomass burned and emission factors (EFs) to provide daily fire emissions at 1-km resolution (Wiedinmyer et al., 2011). However, FINNv1.5 only includes emissions from the combustion of above-ground vegetation. Therefore, it does not include emissions from combustion of peat. Kiely et al. (2019) added the emissions from the combustion of peat across Indonesia, to create FINNpeatSM. Details on the method can be found in Kiely et al. (2019). In summary, to add emissions from peat combustion they use a 2-step process. First, they use a peatland distribution map to identify where a fire occurred on peatland. For each fire occurring on peatland they add additional emissions from the peat burning using Eq 1:

$$E_s = BA \times BD \times \rho \times EF_s \tag{1}$$

where  $E_s$  is the emissions of a species (s) from an individual fire that occurred on peatland, BA is the burned area and BD is the burn depth,  $\rho$  is the peat density and EF<sub>s</sub> is the emissons factor of a species (s).

The second step of the method was to scale burn depth relative to soil moisture (from the ESA CCI Soil Moisture Product New Version Release (v04.4): ESA CCI SMv04.4). This step accounts for burn depth increasing as peat dries out and the water table decreases. In FINNpeatSM burn depth is assumed to increase linearly between a minimum of 5 cm to a maximum of 37 cm. Kiely et al. (2019) used soil moisture from ESA CCI SMv04.4, which provided soil moisture retrievals up to 2018. To extend the FINNpeatSM dataset to 2023, Graham et al. (2024) updated the method to use the SMAP level 4 product. In the





Level 4 dataset, SMAP measurements of soil moisture in the top 5 cm of the soil column are combined with estimates from a land-surface model. This provides soil moisture in the top 1 m of the soil column. The SMAP is both spatially (9 km) and temporally (3-hourly) complete, the 3-hourly data were aggregated to generate daily-mean values. Daily-mean SMAP values are used to linearly scale the burn depth between a minimum soil moisture of 0.5 m<sup>3</sup>m<sup>-3</sup> (5 cm burn depth) and 0.1 m<sup>3</sup>m<sup>-3</sup> (37 cm burn depth). In this study, we use this version of FINNpeatSM to explore changes in fire burn depth and emissions between 2015, 2019 and 2023.

## 2.4.3 VIIRS VNP14IMG Fire Product

The Visible Infrared Imaging Radiometer Suite (VIIRS) active fire product (VNP14IMG) provides the latitude, longitude, time, and a confidence flag for a fire detection pixel. The VNP14IMG product was developed from a MODIS thermal anomaly algorithm which was able to detect fires at a 1 km spatial resolution. VIIRS fire products are provided at 375 m, a much higher spatial resolution compared to MODIS, and therefore VIIRS is able to detect small wildfires that MODIS is insensitive to. Only nominal and high confidence fires during nighttime were included in this work.

## 3 Results

190

195

## 3.1 HCN emissions during the 2015 Indonesian fire season

## 3.1.1 Satellite observations of HCN in 2015

IASI satellite observations are used to estimate the amount of HCN emitted from the Indonesian region during the 2015 wildfire season; the plume of HCN emitted during the wildfire season is clearly visible in the right panel of Figure 1. In Section 3.2, we compare these observations with those made during the more recent 2019 and 2023 burning seasons, which also occurred during El Niño years.

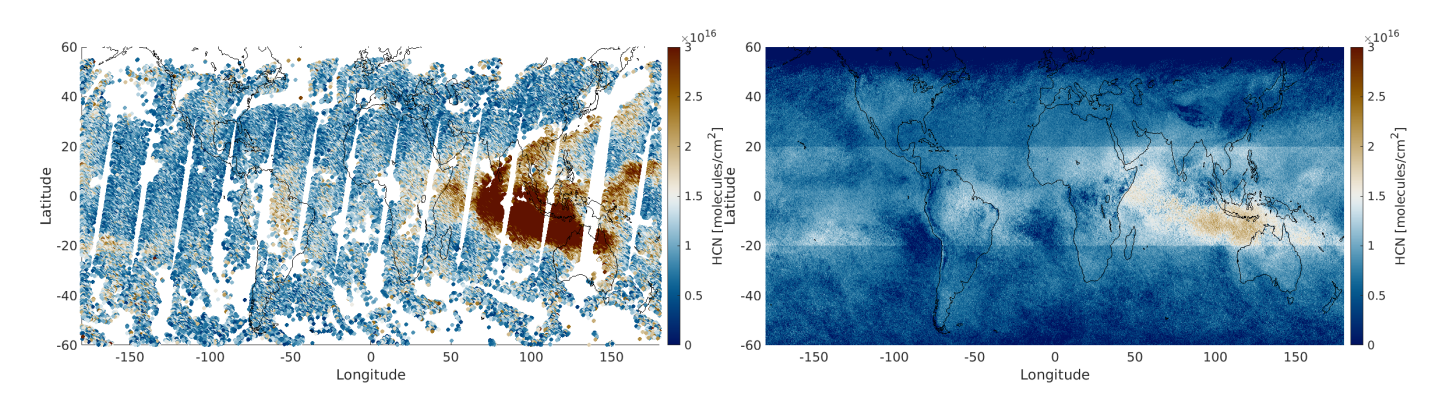


Figure 1. IASI global distribution of HCN total column (molecules cm<sup>-2</sup>) as retrieved by ULIRS for (a, left) 1 November 2015 during daytime and (b, right) the November 2015 monthly mean regridded on a  $0.25^{\circ} \times 0.25^{\circ}$  grid.





210

According to the new peatland fire stages classification — stage 1 surface fire, stage 2 shallow peatland fire (depth < 20 cm) and stage 3 deep peatland fire (depth > 20 cm) — proposed by Hayasaka et al. (2020), the Indonesian fires of 2015 were classified as stage 2 for the second half of August and stage 3 from early September to the end of October. This is broadly consistent with the averaged total column of the IASI HCN observations seen in Figure 2, where the highest HCN total columns are observed in September and October. The HCN total columns peak in late October / early November, consistent with the work of Nechita-Banda et al. (2018) on CO emissions from the same peat fires. Their results indicate a sudden increase in CO emissions for the latter half of October 2015.

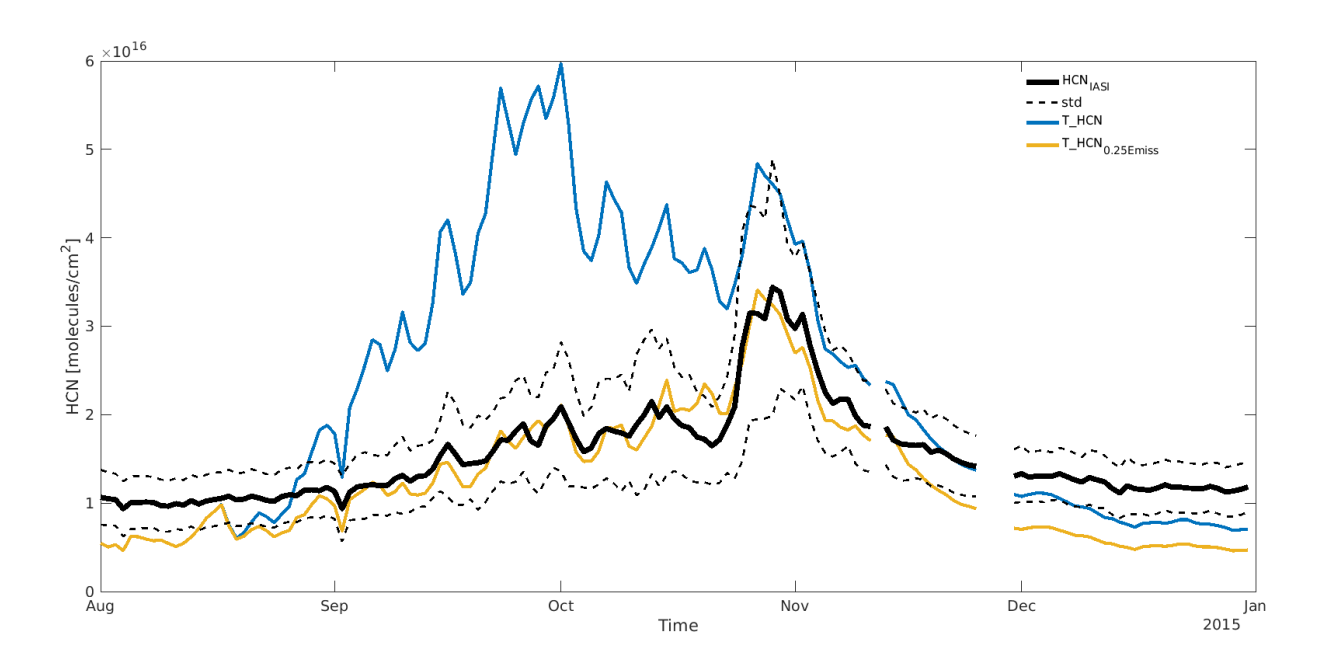


**Figure 2.** Comparison of the IASI measured HCN averaged total column time series (molecules cm<sup>-2</sup>) (black line), and HCN TOMCAT model run using (i) monthly emissions from GFED v4.1 (blue line) and (ii) GFED v4.1 emissions with September values scaled to 25% (orange line). The errors are defined as the standard deviation of the averaged total columns over Indonesia within the region 12°S-7°N and 90°E-127°E.

During neutral conditions, Indonesia is situated under one of the rising branches of the Walker circulation, linked to high rainfall. However, during El Niño, the circulation shifts eastwards and the air over Indonesia tends to sink, resulting in below average rainfall, higher surface pressure, and dryness. A plot of vertical winds at 0° latitude (Indonesia spans 95°E-140°E longitude) derived from ERA5 for October 2015 (Figure 3) demonstrates this; the air mass over Indonesia is primarily descending. At the end of October / beginning of November, the circulation pattern suddenly changes to one in which the air is predominantly being uplifted. This is clearly observed in the top panels of Figure 3, which shows the monthly mean ERA5 vertical wind vectors averaged along the equator for October 2015 and November 2015. The end result is that in late October, HCN from the peat fires is more readily uplifted to higher altitudes, coinciding with the region of the atmosphere where the





IASI sensitivity is greatest. In addition to the increased emissions at the end of October, this contributes to the plume appearing most prominent in the first days of November 2015.

The end of October 2015 also coincides with the onset of increased precipitation and an increase in soil moisture. Figure 4a shows that Indonesian deep soil moisture (SWI at the lowest layer corresponding to the characteristic timelength T=100, described in Section 2.3.2) for August - October 2015 was at its lowest level over the last decade, with a minimum at the end of October. The choice of the parameter T=100, the lowest layer of SWI, allows us to evaluate the water availability at the plant root depth. This strongly suggests that the GWL during the 2015 El Nino season was at a lower level than in any other year over the last decade. Precipitation for the same period was at the lower end of typical values for the given months as shown in Figure 4b using IMERG data.

## 3.1.2 Evaluation of 2015 Indonesian HCN emissions using TOMCAT model simulations

In order to estimate the HCN emissions from the 2015 Indonesian peat fires, retrieved HCN total columns from IASI are compared with outputs of a tracer version of the TOMCAT 3D CTM.

This version of the model makes use of the best-fitting ocean uptake scheme defined in Bruno et al. (2023), the Li et al. (2000) fluxes reduced by 75% and the reaction rates proposed by Kleinböhl et al. (2006) for HCN oxidation by OH radicals and  $O(^1D)$ . Outputs for 2015 were simulated on a horizontal  $2.8^{\circ} \times 2.8^{\circ}$  (T42 Gaussian) grid on 60 terrain-following vertical levels (surface to  $\sim$ 60 km) for HCN. In order to compare the model output (T\_HCN) with the IASI daily measurements over a short time period, the model was sampled daily and adapted for use with the monthly GFED v4.1 inputs for HCN biomass burning emissions. The TOMCAT model reads the emissions as monthly means, which are then interpolated in time so that the emissions vary smoothly during the model run.

TOMCAT total columns were constructed from the raw output using the approach proposed by Deeter (2002), in which the model profiles are interpolated onto the ULIRS retrieval grid and smoothed by applying the ULIRS averaging kernels as  $x_{TOMCAT}^{smooth} = x_a + A(x_{TOMCAT}^{int} - x_a)$ , where  $x_a$  is the a priori profile, A the retrieval averaging kernel matrix, and  $x_{TOMCAT}^{int}$  the model profile interpolated onto the retrieval grid.

Figure 2 compares the averaged total column time series of HCN, calculated over Indonesia in the regional box  $[12^{\circ}\text{S}-7^{\circ}\text{N}, 90^{\circ}\text{E}-127^{\circ}\text{E}]$  for both IASI measurements (black line) and the TOMCAT model outputs smoothed using the IASI averaging kernels (blue line). The T\_HCN model run does not compare very well with the IASI measurements, showing a large overestimation of the HCN amount during the period between September and November 2015. In particular, the large peak observed for T\_HCN during the last week of September is completely absent from the IASI measurements. The left panel of Figure 6 shows the HCN total column distribution on 2 November 2015 produced from T\_HCN. The HCN amount produced is globally overestimated compared with the IASI measurements reported in Figure 1, in particular over the latitude band between  $20^{\circ}$  N and  $40^{\circ}$  S. The discrepancy observed between the HCN TOMCAT model and IASI measurements is seemingly caused by the HCN emissions used to drive the model, shown in Figure 5, which combine GFED v4.1 (the main component), CMIP6 and CCMI as described in Bruno et al. (2023). These emissions indicate an anomalously large peak of more than  $4 \times 10^{11}$ 





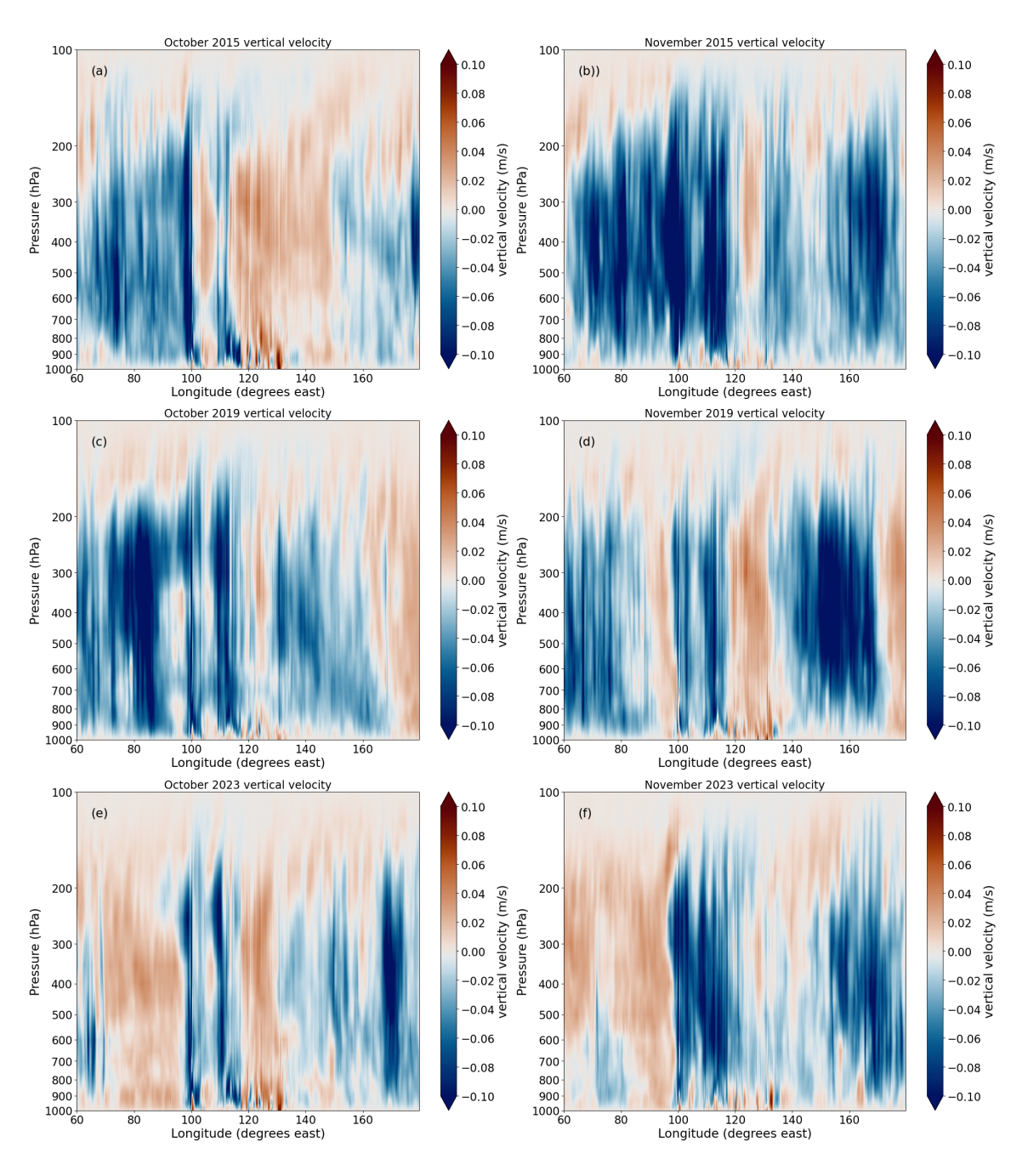


**Figure 3.** Monthly mean ERA5 vertical wind vectors (m  $\rm s^{-1}$ ) averaged along the equator for (a) October 2015, (b) November 2015, (c) October 2019, (d) November 2019, (e) October 2023, and (f) November 2023. Red (blue) areas indicate where, on average, the air is descending (ascending) for that particular month.





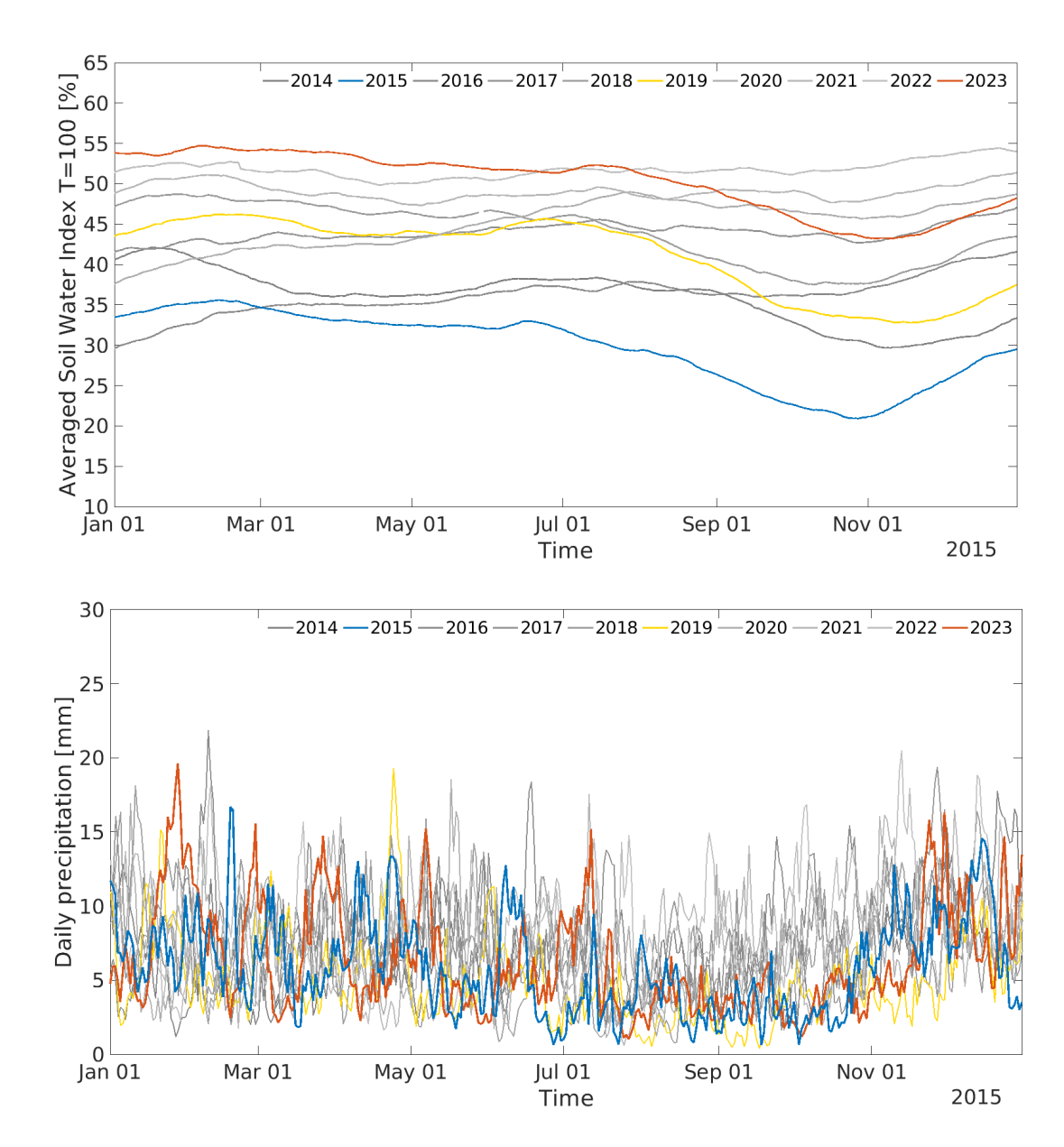


**Figure 4.** (a, top) Averaged Soil Water Index (SWI) T=100, over Indonesia in the period 2014-2023. (b, bottom) Daily accumulated precipitation (combined microwave-IR) averaged over Indonesia estimate from the Integrated Multi-satellitE Retrievals for GPM (IMERG) in the period 2014-2023.

molecules  $cm^{-2} s^{-1}$  in September 2015. This value is more than double the October emissions, during which the largest HCN concentrations were observed over Indonesia during the 2015 wildfire season.





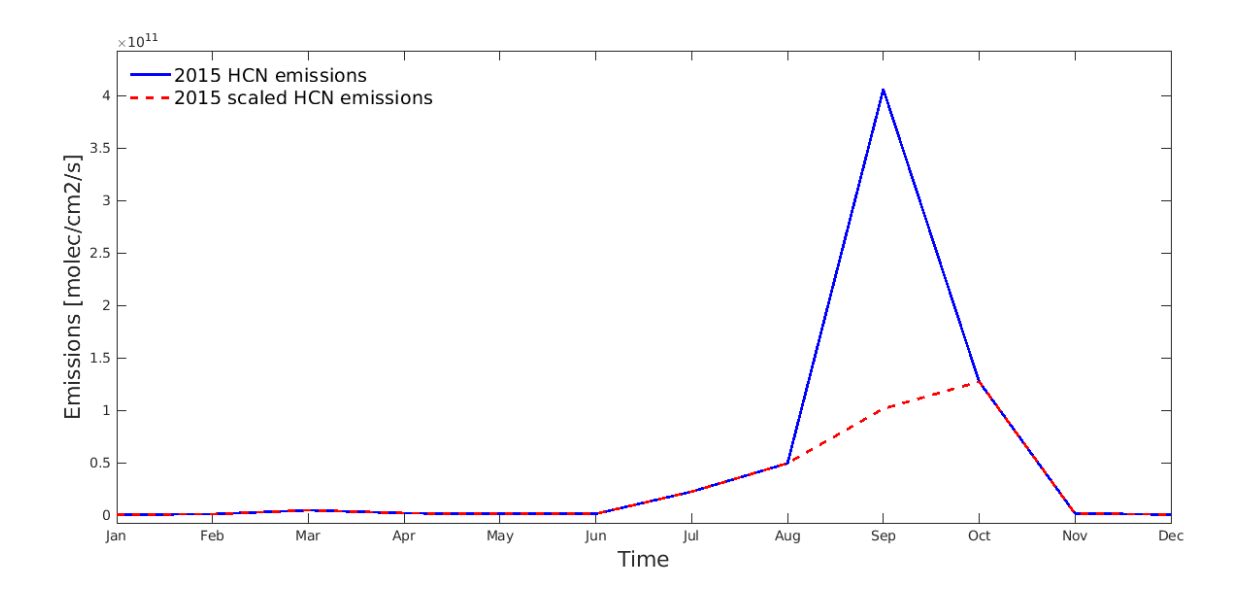


Figure 5. Monthly average HCN 2015 emissions (molecules cm<sup>-2</sup> s+-1) based on GFED v4.1 used in the T\_HCN TOMCAT model experiment (blue line) compared with the scaled emissions used in the T\_HCN<sub>0.25Emiss</sub> experiment (red dashed line).

In order to seek better agreement between model and observations, we performed a number of model sensitivity runs. These suggested that the most sensitive component for improving the model simulations was the September GFED HCN emissions. For this reason, a new model run was performed (T\_HCN<sub>0.25Emiss</sub>) in which the September 2015 emissions were reduced by 75%. The orange line in Figure 2 indicates the averaged total column (smoothed by the IASI HCN averaging kernels) over Indonesia for the T\_HCN<sub>0.25Emiss</sub> model run, showing a substantial reduction in HCN concentration during September and October and reaching a very good agreement with the IASI measurements. However, the background HCN values, e.g. in December, are underestimated in the model, possibly due to neglect of additional sources. The global HCN total column distribution modelled on 2 November 2015, as shown in the bottom right panel of Figure 6, shows a significantly improved agreement with the IASI measured HCN total columns in Figure 1.

The study of CO emissions from the 2015 Indonesian wildfire season by Nechita-Banda et al. (2018) found that GFED is not good at reproducing emissions from large peat fires. GFED estimates monthly fire emissions from satellite-observed burned area and temporally disaggregates them within each month using fire radiative power as a proxy for combustion intensity and timing. For peat-dominated fires, burned area is more sensitive to the initial burning stages and less sensitive to peat burning that occurs underground. Our work supports this conclusion with respect to emissions of HCN from peat fires.

### 3.1.3 Enhancement ratios and emission factors

260

265

The Indonesian peatland fires from 2015 present an opportunity to estimate the HCN wildfire emission factors from satellite data. The fires burned for several months over a limited area, with the prevailing wind conditions resulting in the emitted





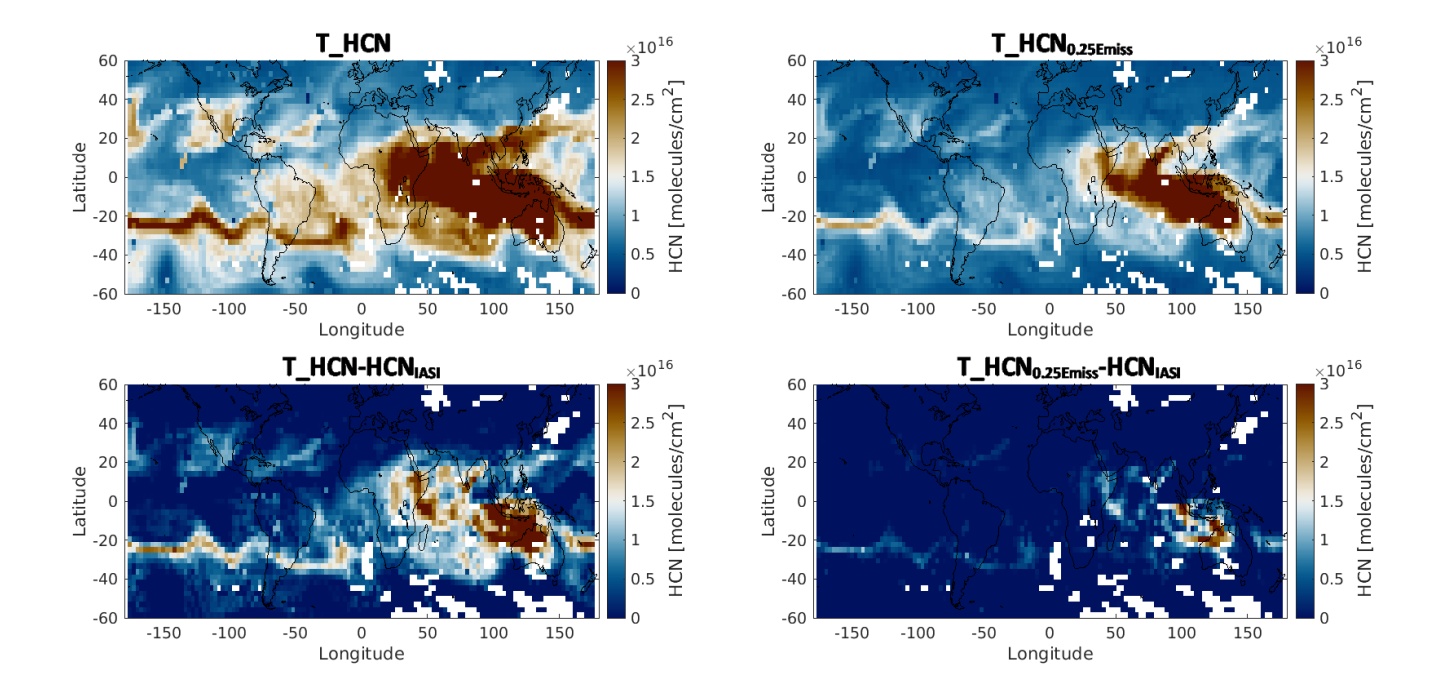


**Figure 6.** Global distribution of HCN total column (molecules cm $^{-2}$ ) on 2 November 2015 produced from (a, top left) T\_HCN and (b, top right) T\_HCN $_{0.25Emiss}$ . The bottom panels shows the total column difference between the two runs and the IASI measurements regridded on the TOMCAT grid.

plumes being predominantly transported over the Indian Ocean. The relatively long lifetimes of HCN and CO, of the order of 2-5 months, allow us to take advantage of satellite measurements over the ocean, where surface emissivity is reasonably homogeneous, and where the polluted air has been uplifted to higher altitudes, corresponding to the maximum sensitivity of IASI to HCN and CO perturbations. Changes in thermal heating over land between day and night cause a change in vertical sensitivity of IASI to HCN and CO. The effect over the oceans is much smaller due to the larger heat capacity of water. As such, in this work we use an average from both IASI daytime and night time measurements to maximise coverage and reduce the random uncertainty of the results.

The emission factor (EF<sub>X</sub>) is a quantity defined as the mass of a trace gas (X) emitted per kilogram of biomass burned (g kg<sup>-1</sup> dry matter). In order to derive EF<sub>X</sub>, it is first necessary to derive a related parameter called the enhancement ratio (ER) which can be determined directly from satellite measurements. The ER<sub>HCN/CO</sub> is defined as a ratio of the emitted number of molecules of HCN over the emitted number of molecules of CO (Goode et al., 2000; Whitburn et al., 2017),

$$ER_{HCN/CO} = \frac{[HCN]_{smoke} - [HCN]_{background}}{[CO]_{smoke} - [CO]_{background}}.$$
(2)



280

285

290

295



CO is chosen as the reference gas in this work as it has a similar lifetime to HCN and is emitted from similar sources. The excellent daily coverage of IASI allows a daily estimation of ER<sub>HCN/CO</sub> to be performed. We have chosen the region 12°S-7°N, 90°E-127°E, located downwind of the Indonesian emissions from Sumatra and Kalimantan; only data with a correlation coefficient greater than 0.3 are included in our analysis. There is no clear trend in the ER across the September 2015 to December 2015 period (Figure 7), although there is some variability with lower ER in early September, where the correlation between HCN and CO measurements is less than 0.4. The phase of fire is a key factor in the emission of pyrogenic species. HCN and CO emissions are generally higher during the smouldering phase of fire (lower FRP) with smouldering peat fire emission factors being approximately 10 times those of flaming savanna fires (Hu et al., 2018). Peat fires generate weakly buoyant smoke plumes (Hu et al., 2019) that generally accumulate close to the ground, although the emissions can migrate great distances via the prevailing winds. The lower ER in early September may be due to the fact that the fires were only recently ignited and high HCN (and CO) levels were closer to the ground. IASI is more sensitive to near surface CO than HCN, so HCN is likely underestimated at that time. Throughout October, the HCN:CO relationship shows correlation coefficients greater than 0.4. By early November, the fire activity ended abruptly, but the correlation remains greater than 0.3 throughout most of November, until the HCN levels drop below the sensitivity of the IASI instrument.

It is estimated that 90% of fire emissions from the late 2015 fire events were dominated by emissions from peat soils (Whitburn et al., 2017), with the remaining 10% from tropical forest. Using a range of ERs derived for differing correlation coefficients, we are able to estimate HCN emission factors,  $EF_{HCN/CO}$ , from the derived  $ER_{HCN/CO}$ . Since we are investigating a region close to the emissions, and are not influenced by transport from other regions, the two parameters are related by the equation

$$EF_{HCN} = ER_{HCN/CO} \times \frac{MM_{HCN}}{MM_{CO}} \times EF_{CO}.$$
(3)

The quantities  $MM_{HCN}$  (27.0253 g/mol) and  $MM_{CO}$  (28.01 g/mol) are the molar masses of HCN and CO, respectively. There are a number of datasets of  $EF_{CO}$  for peat over Indonesia (Table 1). Stockwell et al. (2016) measured  $EF_{CO}$  in situ (291 $\pm$ 49 g kg $^{-1}$ ), noting that their measurements were solely from smouldering combustion. Huijnen et al. (2016) also measured  $EF_{CO}$  in situ (255 $\pm$ 39), but noted a few smoke measurements involved occasional contributions from small clumps of ignited dry vegetation, which may account for the smaller value of  $EF_{CO}$ . More recently, Yokelson et al. (2022) revisited Kalimantan in 2019, during El Nino conditions, to sample fires burning only peat and measured a 50% larger  $EF_{CO}$  compared to the Stockwell et al. (2016) work in a similar region. Both Christian et al. (2003) and Stockwell et al. (2016) took samples from Sumatra and Kalimantan respectively and burned the samples in the lab, both deriving significantly lower  $EF_{CO}$  values. The final source is from a meta-analyses study by Rodriguez Vasquez et al. (2021) who use the data from the in situ and laboratory studies previously listed to derive an updated  $EF_{CO}$  based on methodological differences in measurements and weighted to account for different sample sizes.

© Author(s) 2025. CC BY 4.0 License.



320

330



**Table 1.** Emission factors,  $EF_{HCN}$ , in g kg<sup>-1</sup> dry Matter derived from the calculated  $ER_{HCN/CO}$  and various CO EFs from the literature.  $EF_{HCN}$  is presented for increasing correlation coefficients of HCN:CO total column measurements over the box [12°S-7°N, 90°E-127°E].

Author	study area	Measurement	EF <sub>CO</sub> (g kg <sup>-1</sup>	EF <sub>HCN</sub> r	EF <sub>HCN</sub> r	EF <sub>HCN</sub> r	EF <sub>HCN</sub> r
		type	DM)	> 0.5	> 0.6	> 0.7	> 0.8
Yokelson et al. (2022)	Kalimantan	In situ	315±49	1.66±0.76	$1.87 \pm 0.80$	2.41±0.80	2.50±0.55
Rodriguez Vasquez et al.	N/A	Meta-analyses	258.68±15.34	1.33±0.50	1.50±0.52	1.95±0.47	2.04±0.26
(2021)							
Stockwell et al. (2016)	Kalimantan	In situ	291±49	1.54±0.72	$1.73 \pm 0.76$	2.23±0.77	2.32±0.54
Huijnen et al. (2016)	Kalimantan	In situ	255±39	1.35±0.61	1.51±0.64	1.95±0.64	2.03±0.44
2016							
Stockwell et al. (2014)	Kalimantan	Laboratory	233±72	1.29±0.74	$1.44 \pm 0.80$	1.83±0.86	1.87±0.69
Christian et al. (2003)	Sumatra	Laboratory	210.3	1.06±0.34	$1.20 \pm 0.35$	1.56±0.29	1.66±0.11

Examining the relationship between HCN and CO total column amounts in Figure 7, the correlation coefficient between the two species varies between 0.3 and 0.8 over most of the September to November 2015 period. Generally the lower correlation coefficients are associated with lower ER values. The effect on estimating  $EF_{HCN}$  by including only measured data exceeding a chosen correlation coefficient threshold is shown in Table 1. The highest  $EF_{HCN}$  values are derived where the correlation coefficient exceeds 0.8, ranging between 1.66 and 2.32 g kg<sup>-1</sup> depending on which value is used for  $EF_{CO}$ . Where the correlation coefficient HCN:CO is greater than 0.5, we see that the  $EF_{HCN}$  estimates decrease, ranging between 1.06 and 1.54 g kg<sup>-1</sup>. Both ends of the estimates are lower than the (surface) in situ and lab-based estimates of  $EF_{HCN}$ . We know that the IASI HCN sensitivity is in the upper troposphere between 8 and 12 km, with very low sensitivity to high concentrations below 4 km. Field et al. (2016) show that the MLS CO at 215 hPa ( $\sim$ 12 km) increased steadily through September with a rapid increase to CO exceeding 400 ppbv at the end of October. The highest correlation HCN:CO in our results is during this late October period, where we see enhanced vertical uplift of both gases and therefore increased sensitivity to the HCN emissions. Before mid-October, we likely underestimate the HCN amounts as plumes are closer to the surface.

#### 3.2 Comparison of the 2015 Indonesian fire season with the 2019 and 2023

According to the ONI, the 2015 El Niño event was one of the strongest in the satellite era. ONI is the de-facto standard used by NOAA for classifying El Niño events. Defined as a running 3-month mean sea-surface-temperature anomaly for the Niño 3.4 region (5°N-5°S, 120° -170°W), El Niño events are defined as 5 consecutive overlapping 3-month periods above +0.5°. Figure 9 shows a plot of ONI as a function of time since 1990. It indicates that the recent 2023 burning season in Indonesia, also occurring during an El Niño event, peaked at the third strongest ONI value since 1990, behind only the 1997 and 2015 events. The 2019 event was comparatively weak.

In order to compare fire activity in Indonesia during the last three El Niño events, in late 2015, 2019 and 2023, we use the 375 m resolution fire product (VNP14IMG) measured by the VIIRS sensor on the Suomi-National Polar-Orbiting Partnership



335

340

345



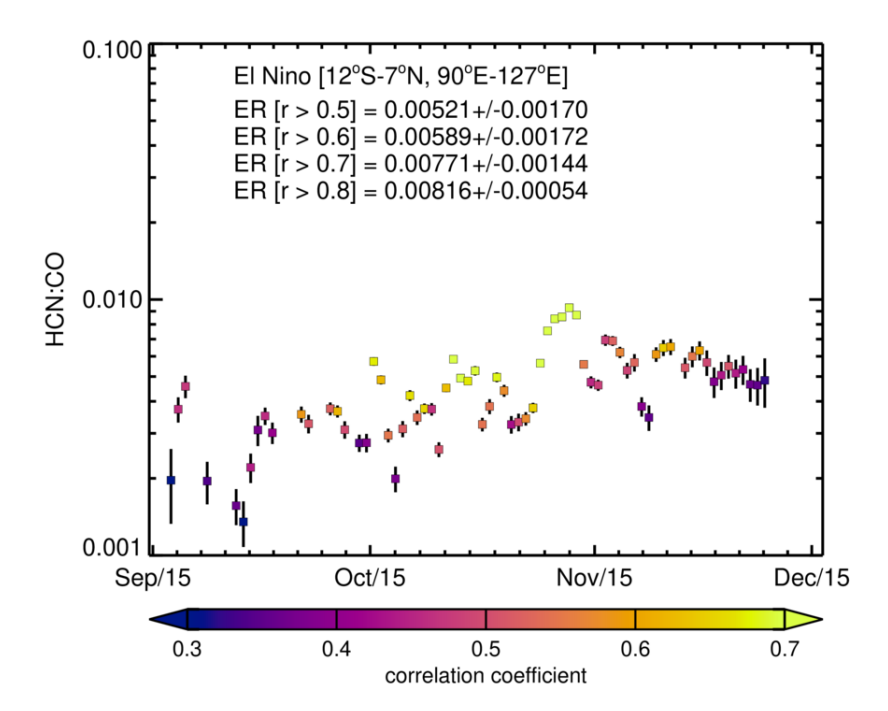


**Figure 7.** Daily HCN enhancement ratios (ER) relative to CO calculated from the slope of the linear regression of HCN against CO total columns between 1 September and 1 December 2015, over the Indian Ocean (12°S-7°N, 90°E-127°E). The error bars correspond to the standard errors on the regression slope. Any data with a correlation coefficient <0.3 for the slope have been excluded.

(S-NPP) satellite. This product provides information on fire geolocation (latitude, longitude) with a confidence flag; here we use only information scenes with nominal and high confidence flags. The VNP14IMG product is a development of the MODIS thermal anomaly algorithm and several studies have now shown (Schroeder et al., 2014; Zhang et al., 2017) that it is capable of detecting small fires which MODIS does not have the sensitivity to measure. In this study, we selected the VNP14IMG fire product across the whole 2012 to 2023 period and look at the total fire activity across all of the Indonesian islands. Cumulative monthly fire radiative power over Indonesia is plotted in Figure 11, and indicates that even during a notably strong El Nino phase, the fire activity in 2023 was almost eight times less than in 2015. Specifically in 2023 the fire activity was below the seasonal 2012-2023 average across the whole July-December period. For 2019, we observe significant fires in mid-September and a comparable increase in fire power to 2015 between early September and late September. From late September 2019, the fire activity abruptly ends, whereas 2015 maintains a steady increase in fire cumulative power until an abrupt end in fire activity in late October 2015.

We can use the ULIRS HCN to further investigate the emissions from the Indonesian peat fires. Figure 8 represents a 3-day simple moving average total burden HCN (in Gg) for the three El Nino years. The total mass was calculated over the region 12°S-7°N, 90°E-127°E, and shows the highest values are towards the end of October 2015. Comparing all three years used in this study, we see the highest HCN values across the September to November period always occur in 2015. The HCN





350

355

360

concentrations increase in early September 2015 and are shown to be coincident with an increase in fire activity during the same period (Figure 11), rapidly exceeding 500 Gg by 25 September. After this period we see the largest increase in HCN between 22 October and 30 October, to approximately 600 Gg of HCN, peaking at 1125 Gg on 29 October. This increase can also be linked to increasing fire power over that period, although we note that the increase in fire power is also conducive to extra lofting of the elevated HCN to altitudes where the IASI instrument is more sensitive to HCN changes (i.e. the upper troposphere). After 1 November, concentrations decrease for the remainder of 2015. For 2019, the pattern in early September mirrors that in 2015 with a sudden increase of 0.24 Gg of HCN between 3 September and 26 September. After that, HCN concentrations decrease back to the 0.3 baseline by 9 October and stay at these lower levels for the rest of 2019. In 2023, we observe no significant enhancements in HCN across the August to December period, relative to the 300 Gg baseline.

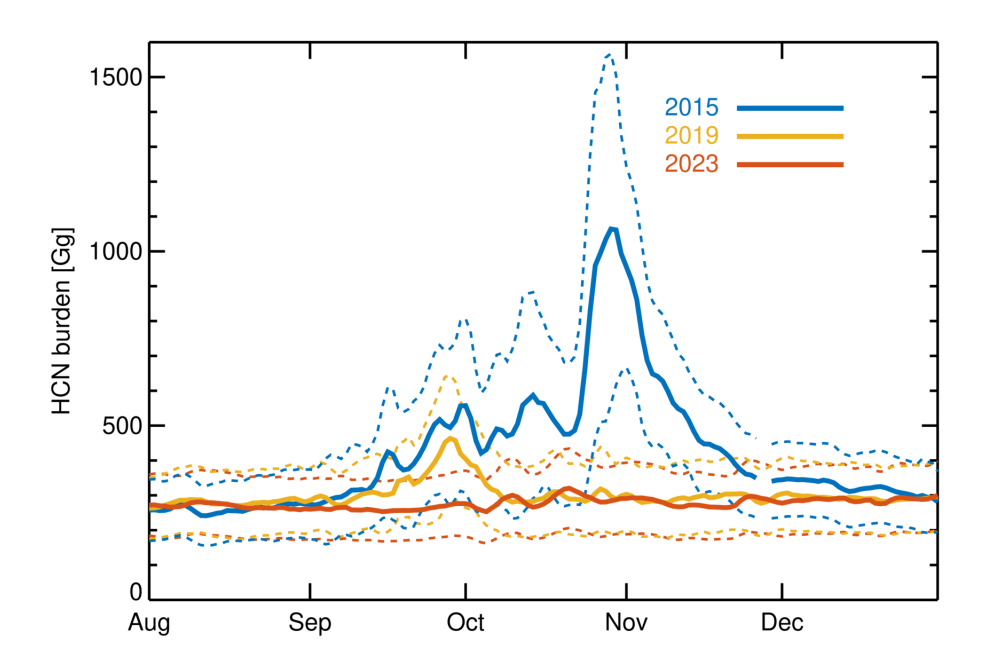


**Figure 8.** Daily Infrared Atmospheric Sounding Interferometer (IASI) derived HCN burden (Gg) between the 1 August and 31 December for three years: 2015 (blue line), 2019 (yellow line), and 2023 (red line). This is calculated for the region 12°S-7°N, 90°E-127°E.

Comparing the circulation patterns across the equator in October 2015 and 2023 in Figure 3, it is clear that the regimes are quite different, with the descending air over Indonesia in 2015 replaced by more neutral conditions in October 2023. These conditions are less conducive to prolonged dry periods, which would allow peat fires to establish if left unchecked. Over the western Pacific Ocean itself, October 2023 showed much less wide-scale descent of air compared to 2015, suggesting that the Walker circulation did not weaken significantly in late 2023. The circulation patterns across the Eastern Indian Ocean (60°E-110°E) in October 2015 and October 2019 are remarkably consistent. Over Indonesia itself (100°E-120°E) the vertical winds exhibit very different behaviour between 2015 and 2019, with 2019 conditions more conductive to convection and increased rainfall, which would likely suppress fire activity.





Figure 4b indicates that the precipitation levels in August to October for the El Nino years 2015, 2019 and 2023 were very similar. However, Figure 4a demonstrates that the SWI in the lowest soil layer towards the end of 2019 and 2023 was quite typical of values over the last decade, unlike 2015 which was significantly drier. This is consistent with previous work showing that peat moisture, in particular the GWL, is a major factor in determining the ignition and spread of peat fires (Hayasaka et al., 2020).

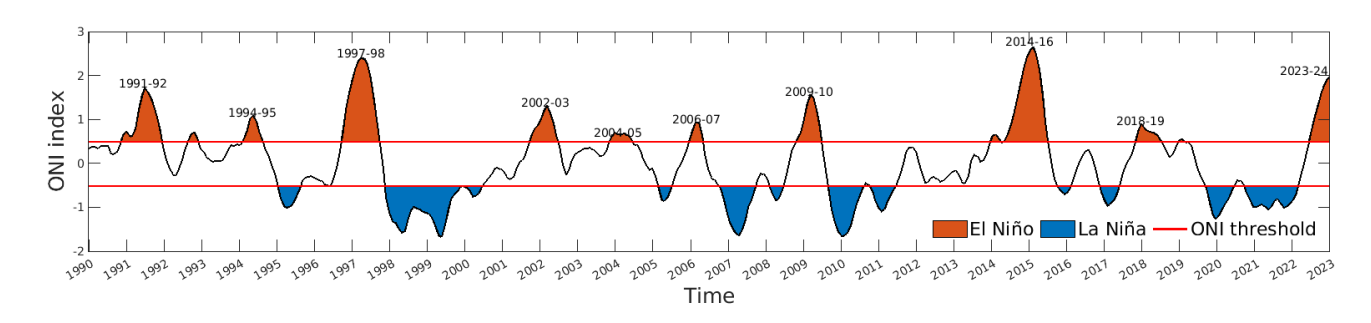
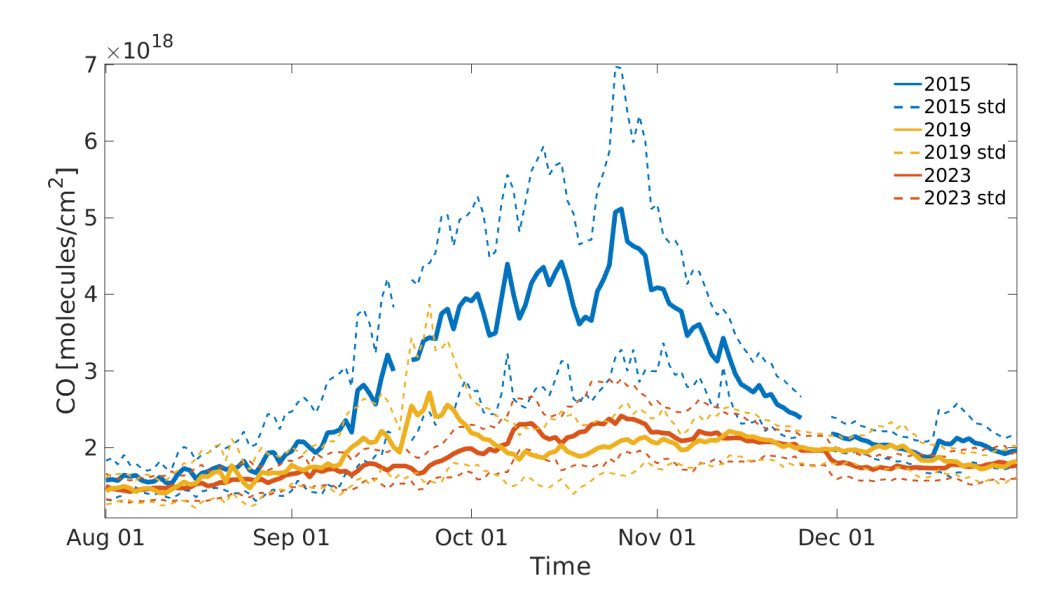


Figure 9. Time series from 1990-2023 of ONI index, with warm (red shaded area) and cold (blue shaded area) periods based on a threshold of  $\pm 0.5^{\circ}$  C.



**Figure 10.** Comparison of the IASI measured CO averaged total column time series for August-December 2015 (blue line), 2019 (yellow line) and 2023 (red line). The errors are defined as the standard deviation of the total column in the box and the averaged total columns are calculated over Indonesia in a box  $[12^{\circ}S-7^{\circ}N, 90^{\circ}E-127^{\circ}E]$ .



380

385



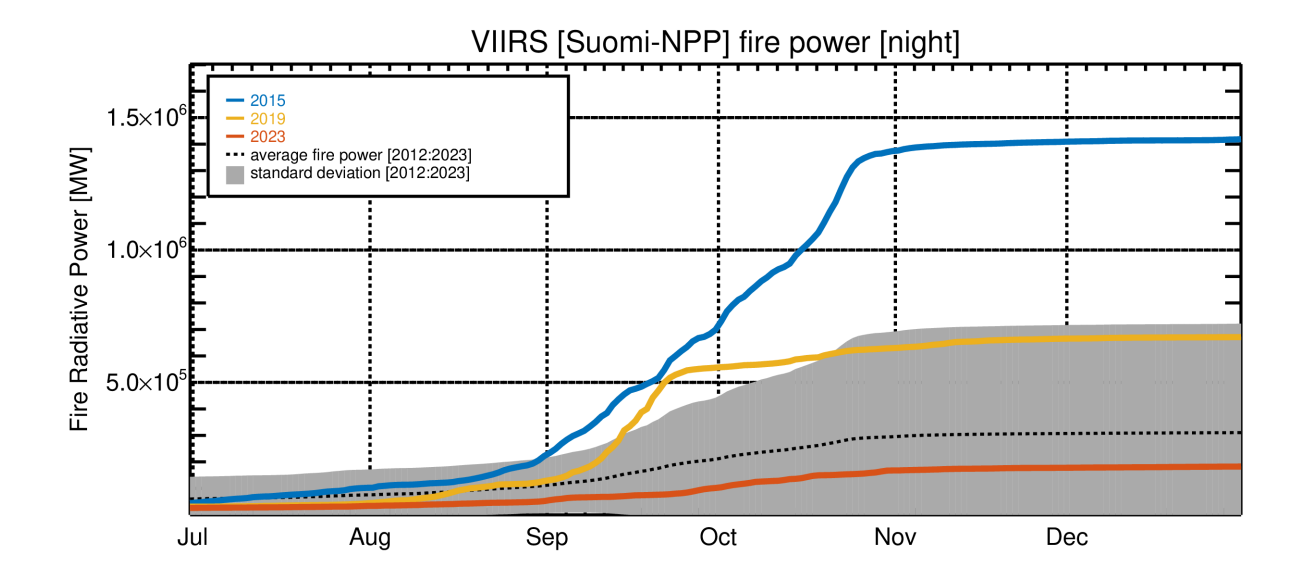


**Figure 11.** Total cumulative monthly fire radiative power (MW) over Indonesia measured by VIIRS. The fire activity in 2023 (red line) is almost eight times smaller than in 2015 (blue line), and falls below the seasonal long-term (2012-2023) mean (black dotted line).

## 3.2.1 HCN emission database fusing the FINNpeatSM method

To explore the drivers of differences in HCN retrievals between 2015, 2019 and 2023 we examine fire detections (from VI-IRS fire hotpots) and Soil Moisture Active Passive Data (SMAP, ONeill et al. (2021)) over Indonesia peatlands. Using the FINNpeatSM method (Kiely et al., 2019), we can combine these datasets to estimate the burn depth of fires in 2015, 2019 and 2023.

Daily VIIRS temperature hotspots are only used if there is a medium or high confidence in the retrieval (Wiedinmyer et al., 2023) and if the fire occurred on peatland in Indonesia. For each retained fire detection, the nearest-neighbour daily mean soil moisture pixel (from SMAP) is determined. The associated soil moisture from an individual fire detection can be used to estimate the burn depth, and emissions, of the fire. The emissions in FINNpeatSM are linearly related to burn depth, so that the deeper a fire burns the higher the emissions.

First, we consider daily mean soil moisture from SMAP across all Indonesian, Kalimantan, and Sumatra peatlands for 2015, 2019 and 2023 (Figure 12). We consider Kalimantan and Sumatra peatlands in addition to all Indonesian peatlands since these regions dominate fire emissions. In 2015 62% of total emissions were from Kalimantan and 33% were from Sumatra (Kiely et al., 2019). Soil moisture is shown for 1 June to 31 December, with the dry season (1 August to 31 October) shaded in grey, since the dry season is when fires are most likely to occur. Across Indonesia and both Kalimantan and Sumatra soil moisture in 2015, 2019 and 2023 were similar from June-July (0.58-0.61 m<sup>3</sup> m<sup>-3</sup>). However, from July to August, soil moisture across all regions in 2015 and 2019 begins to decrease rapidly (from 0.52-0.55 m<sup>3</sup> m<sup>-3</sup> to 0.46-0.48 m<sup>3</sup> m<sup>-3</sup>), while in 2023 soil



390



moisture remains high (0.59 to 0.54 m $^3$  m $^{-3}$ ). From August to mid-September soil moisture continues to decrease across Indonesia, driven by reductions in soil moisture in Kalimantan in 2015 and 2019 (Indonesia from 0.46-0.48 to 0.36-0.39 m $^3$  m $^{-3}$  and Kalimatan from 0.39-0.44 to 0.27-0.29 m $^3$  m $^{-3}$ ). In contrast, over the same period in 2023, soil moisture remains high across Indonesia (decreasing from 0.54 to 0.50 m $^3$  m $^{-3}$ ), driven by high soil moisture in Sumatra peatlands. From mid-September to mid-October soil moisture continues to decrease in 2015 (from 0.39 to 0.33 m $^3$  m $^{-3}$ ), while in 2019 there is an abrupt increase in soil moisture (from 0.36 to 0.47 m $^3$  m $^{-3}$ ), closer to the 2023 values (from 0.50 to 0.54 m $^3$  m $^{-3}$ ). Overall, soil moisture is lowest throughout the dry season in 2015 (1 August to 31 October mean of 0.40 m $^3$  m $^{-3}$ ), while in 2019 soil moisture is very low at the start of the dry season but then increases in the late dry season (1 August to 31 October mean of 0.43 m $^3$  m $^{-3}$ ). In contrast, soil moisture in 2023 is the highest of the 3 years (1 August to 31 October mean of 0.52 m $^3$  m $^{-3}$ ), in agreement with what was observed in SWI data (Figure 4a).

The collocated daily mean soil moisture and daily total number of fire hotspots (from VIIRS) for the same time period (1 June to 31 December 2015, 2019 and 2023) is shown in Figure 13. This clearly indicates that 2015 had the highest number of fire hotspots (>40 collocated pixels with 1,000-10,000 fire hotspots) occurring in areas where soil moisture was low (0.15-0.35 m $^3$  m $^{-3}$ ). However, in 2019, there are fewer fire pixels with a high number of hotspots (24 pixels with 1,000-10,000 fire hotspots) and they generally had higher soil moisture (0.25-0.31 m $^3$  m $^{-3}$ ). In 2023, there were both fewer pixels with a high number of fire hotspots (peaking at 100-1,000 fire hotspots), and the soil moisture where fire hotspots occurred was higher (0.21-0.4 m $^3$  m $^{-3}$ ).

The soil moisture at each fire location can be used to calculate peat burn depth of the fire, using the method developed by Kiely et al. (2019). Figure 14 indicates the burn depth of fires, and the date they occurred. As shown in Figure 13, 2015 has the highest number of fires (up to 25,000 fires) that occur in low soil moisture areas (0.3 m). Figure 14 indicates that these fires burn deep into the peat below (0.25-0.3 m) and occur between September and mid-October 2015 (in line with Figure 12). In contrast, in 2019, there are fewer fires (0-15000), the burn depth is shallower (0-0.25 m), and the fires that burn the deepest occur earlier in the dry season (mid-September) when soil moisture is higher than 2015 (Figure 12). In 2023, far fewer fires (0-5000 fires) burn deep into the peat below (0.05-0.25 m) and deep burning occurs in mid-September to early-October, in line with increased soil moisture in 2023 (Figure 12).

The accumulated daily burn depth of all Indonesian peatland fires from 1 June to 31 December is shown in Figure 15. This plot accounts for both the number of fire hotspots and the burn depth of individual fire hotspots. At the start of the dry season (August to mid-September) the accumulated burn depth in 2015 and 2019 is similar (500-1000 m), compared with <100 m in 2023. This is likely because soil moisture at the start of the dry season (August to mid-September) is similar in both years, and both years have a similar number of fire hotspots at this time. However, from mid-September, 2015 and 2019 deviate. Accumulated burn depth remains high in October 2015, whereas it substantially decreases in 2019. This is likely driven by the large decrease in both fire hotspots and peatland soil moisture in 2019, compared with 2015 where the number of fire hotspots remains high and the peatland soil moisture remains low.





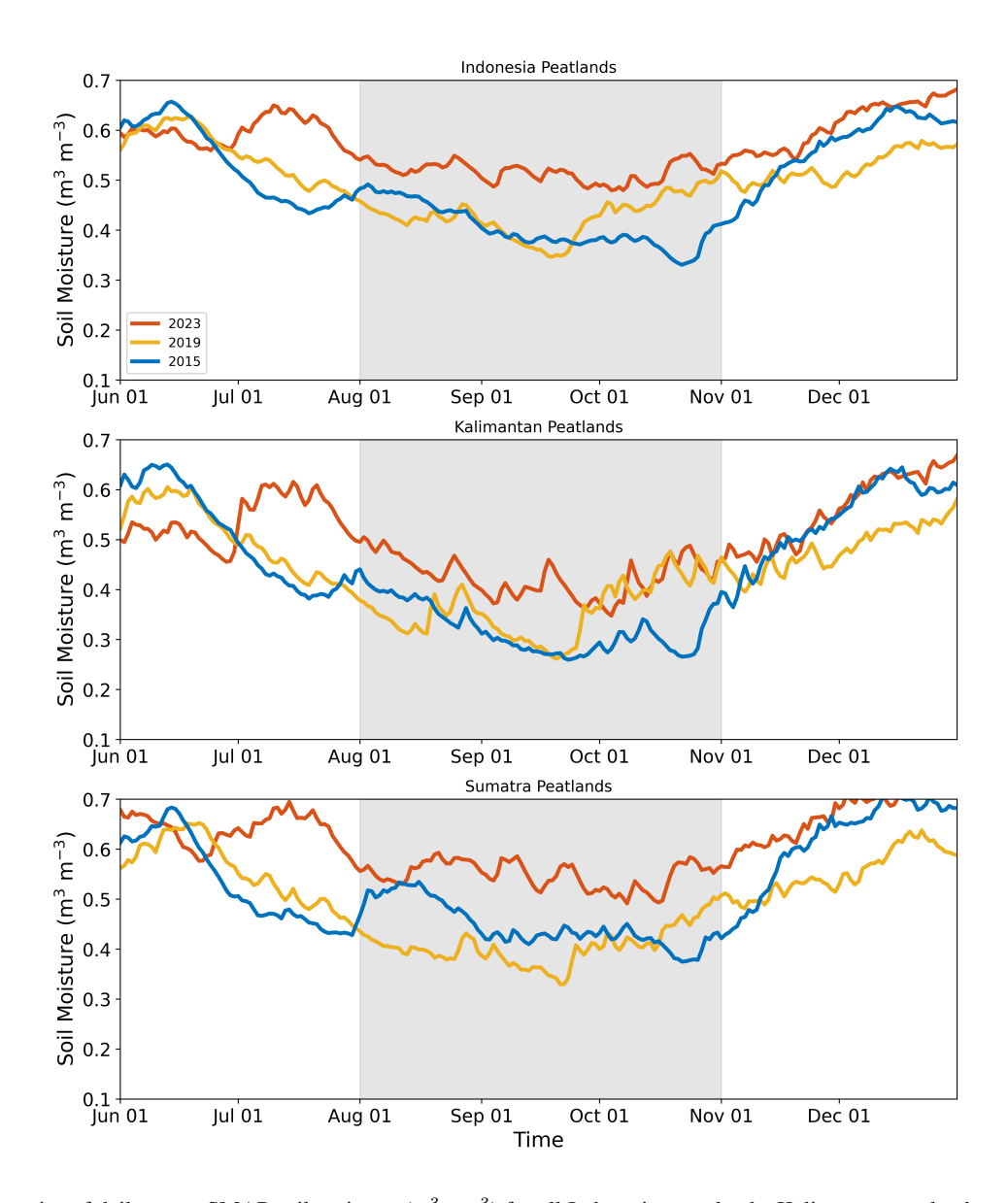


**Figure 12.** Timeseries of daily mean SMAP soil moisture (m<sup>3</sup> m<sup>-3</sup>) for all Indonesian peatlands, Kalimantan peatlands and Sumatra peatlands for 2015 (blue), 2019 (yellow) and 2023 (red) for the period 1 June to 31 December in years 2015, 2019 and 2023.

As illustrated in Figure 16, the time series of accumulated daily burn depth, along with the averaged total column of HCN and CO, exhibit similar temporal patterns, a progressive increase from August through October, reaching a peak in late October, and subsequently declining sharply in November.

A cross-correlation analysis between the accumulated daily burn depth and the total column concentrations of CO and HCN provides insights into the temporal dynamics of plume transport. As shown in Figure 17, both HCN and CO exhibit maximum





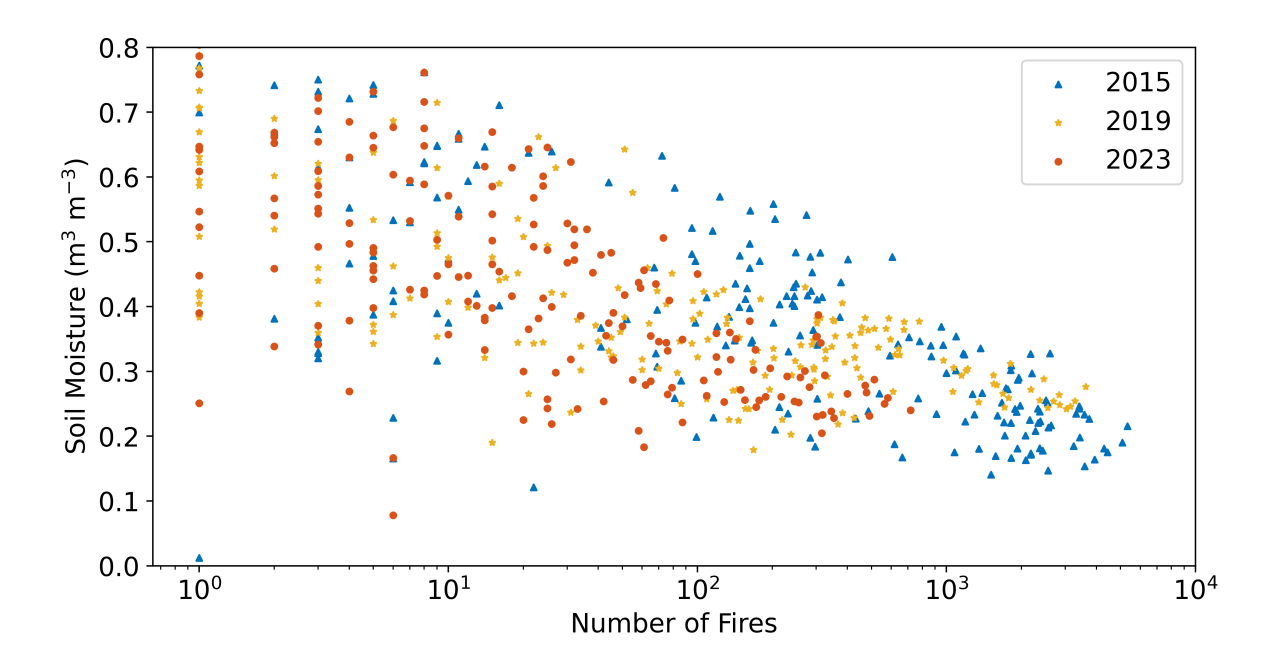


Figure 13. Daily Indonesian peatland fire count (from VIIRS) and collocated daily soil moisture ( $m^3 m^{-3}$ ) for the period 1 June to 31 December in years 2015 (blue triangles), 2019 (yellow stars) and 2023 (red circles).

positive correlations with the burn depth at non-zero lag times, indicating a delay between fire activity at the surface and the appearance of enhanced trace gas signals at the altitudes most sensitive to the IASI instrument. Specifically, the cross-correlation peaks at a lag of approximately 10 days for both species, suggesting that this is the typical timescale required for emissions from peatland fires to be transported and mixed into the mid- to upper-tropospheric layers, where IASI's sensitivity to HCN and CO is greatest.

The cross-correlation function (XCF) for HCN (black line) and CO (orange line) displays a broadly similar temporal structure, with both curves rising steadily from negative lag values, peaking near +10 days, and subsequently declining into negative correlation at higher lag values. The slightly larger peak for CO may reflect differences in vertical transport dynamics or sensitivity profiles, given that CO exhibits dual sensitivity in both the lower and upper troposphere, whereas HCN is primarily sensitive to the mid-troposphere (~10–12 km) (Moore et al., in Preparation). These results support the interpretation that the observed trace gas enhancements are closely linked to fire activity and that the lag time to maximum correlation can serve as an estimate of the average vertical and horizontal transport time of the emission plume.

#### 4 Conclusions

425

430

435

This study has provided a comprehensive assessment of Indonesian peatland fire emissions during recent El Niño events, with a particular focus on hydrogen cyanide (HCN) as a tracer of smouldering combustion during peat fires. By integrating IASI





440

450

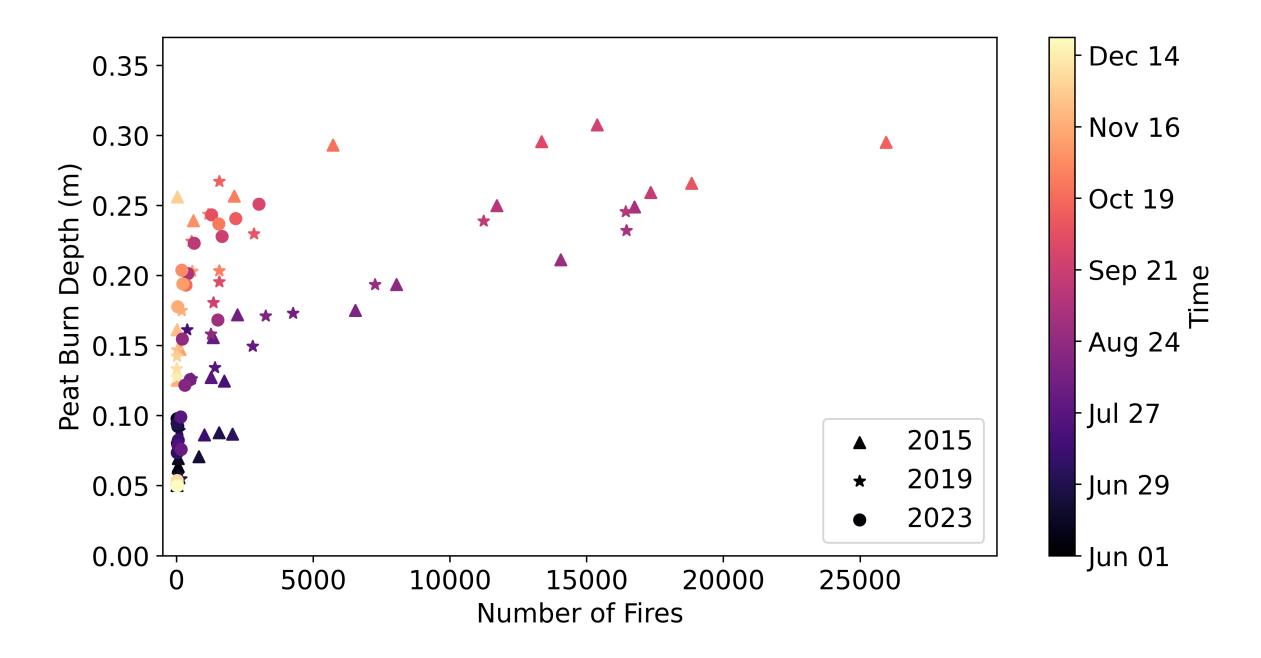


**Figure 14.** Weekly mean burn depth (m) of Indonesia peat fires between 1 June and 31 December in years 2015 (triangles), 2019 (stars) and 2023 (circles).

satellite retrievals with TOMCAT model simulations, precipitation and soil moisture observations, and fire activity datasets, we have quantified both the magnitude and variability of HCN emissions and identified the key drivers underlying interannual differences. The results provide strong evidence that the magnitude of trace gas emissions from Indonesian peatlands is not governed solely by the strength of El Niño but instead arises from the interaction between large-scale ocean—atmosphere dynamics and local hydrological conditions. The 2015 El Niño event, one of the strongest in recent decades, produced exceptionally large atmospheric concentration of HCN and CO, reflecting a combination of extremely low soil moisture, depressed groundwater levels, and deep burn depths in peatlands. The resulting emissions were unprecedented in the observational record, with IASI retrievals showing marked enhancements that were sustained through October and November.

In contrast, the 2019 and 2023 El Niño events, despite also being associated with positive Oceanic Niño Index (ONI) anomalies, resulted in markedly lower HCN burdens related to higher ground water content and atmospheric dynamics that make intense peat fires less favourable. The 2023 event, in particular, occurred under atmospheric circulation regimes that did not sustain prolonged dryness, resulting in fire activity that was nearly an order of magnitude almost eight times weaker than in 2015.

Using IASI total column measurements we also derive new satellite-based emission factors (EFs) for HCN enhancement ratios with CO during the 2015 dry season. These values provide independent, observation-based constraints that can improve the representation of peat fire emissions in models and inventories.



465

470



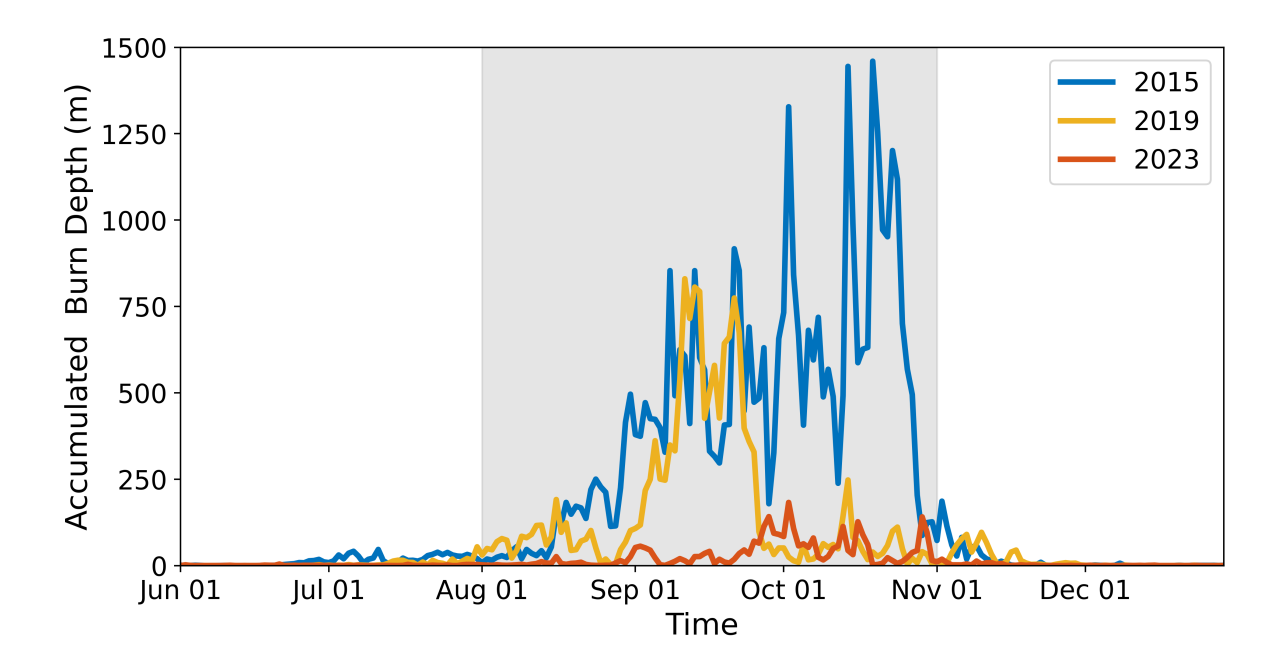


**Figure 15.** Accumulated daily burn depth of Indonesian peatland fires in 2015 (blue), 2019 (yellow) and 2023 (red) between 1 June and 31 December.

Comparisons between IASI-derived HCN total columns and TOMCAT model simulations revealed that standard GFED-based emission inventories substantially overestimate HCN emissions from peat fires during the 2015 dry season, particularly in September. A revised model run, applying a 75% reduction to September emissions, produced much better agreement with satellite observations. This finding suggests that current fire emission inventories underestimate the contribution of peat smouldering processes to trace gas release, as burned-area based definitions used in GFED are poorly suited to capturing the subsurface dynamics of peatland combustion. The analysis also confirms that the new FINNpeatSM approach, which explicitly links burn depth to soil moisture, offers a more accurate description of the dynamics of peat fire emissions.

Hydrological conditions emerged as a dominant control on fire intensity and emissions across all three El Niño events. Soil moisture and groundwater level determine not only the susceptibility of peatlands to ignition but also the persistence of smouldering fires and the total mass of peat carbon released to the atmosphere. When soils are dried, the peat layer can ignite and burn deeply, releasing large quantities of HCN and CO that are transported into the mid- to upper- troposphere within about 10 days. Conversely, higher soil water content suppresses combustion depth and limits the emissions. The strong cross-correlation between accumulated burn depth and satellite-observed HCN and CO concentrations further supports the close coupling between hydrology, fire behavior, and wildfire emissions.

The comparison of 2015, 2019, and 2023 further highlights that fire intensity and trace gas burdens are not determined solely by the strength of El Niño events, but rather emerge from the importance of the local drought intensity, soil moisture deficits, and atmospheric circulation patterns. This underscores the critical role of groundwater and soil moisture in regulating





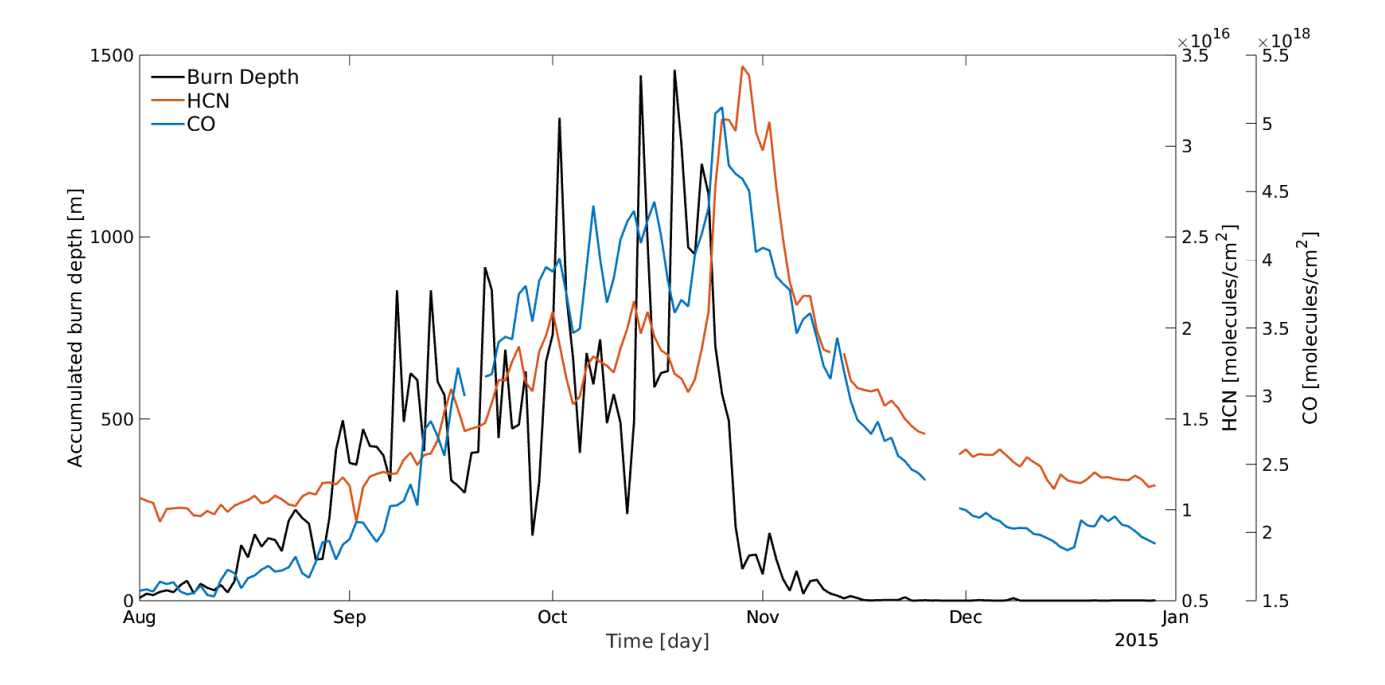


**Figure 16.** IASI measured HCN (red line) and CO (blue line) averaged total column and accumulated daily burn depth (black line) of all Indonesia peatland fires from 1 August to 31 December 2015.

peatland vulnerability to ignition, smouldering persistence, and total emissions. Our results therefore emphasize the need for next-generation emission inventories that explicitly account for soil moisture and groundwater dynamics to better reproduce the peatland fire dynamics. Integrating satellite-derived products of atmospheric composition (e.g. IASI) and soil hydrology (e.g., SMAP, ASCAT, SWI) offers a valuable constrain for emissions and predictions of future fire behavior under changing climate conditions. Such integrated approaches can reduce uncertainties in global fire emission estimates, improve the representation of smouldering combustion in chemical transport models, and enhance the predictive capacity for El Niño-induced fires during the dry seasons across Indonesia peat-dominated ecosystems. These advances are essential for understanding the contribution of peatland fires to regional air quality, global atmospheric composition, and the carbon-climate feedback system.

Data availability. The VNP14IMG product is available from the Level-1 and Atmosphere Archive & Distribution System Distributed Active Archive Center (LAADS DAAC) which archives a number of data archives on Earth atmosphere products for NASA, NOAA and European Space Administration missions. The TOMCAT model data are available at https://zenodo.org/doi/10.5281/zenodo.17194011 (Bruno et al., 2025a) and at https://zenodo.org/doi/10.5281/zenodo.17194064 (Bruno et al., 2025b).





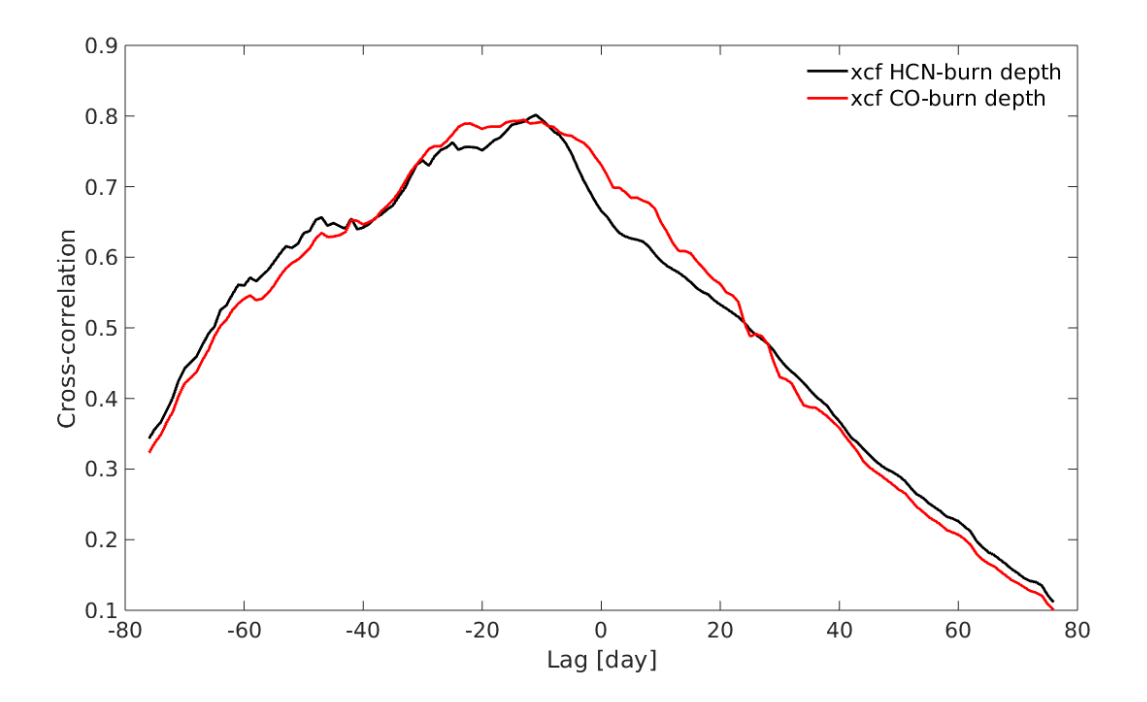


**Figure 17.** Cross-correlation between the IASI HCN total column and the accumulated daily burned depth (black line) and between the IASI CO total column and the accumulated daily burned depth (red line).

Author contributions. This work formed part of the PhD studies of AGB, under the supervision of JJH, DM, and MPC. JJH designed the study, with important contributions from all other co-authors. Most of the data analysis was performed by AGB under supervision of JJH and DM. DM performed the HCN and CO retrievals, and carried out the work on emission factors. AG carried out the FINNpeatSM work. Model runs were performed by AGB under the supervision of MPC. The TOMCAT model is maintained and updated by the MPC research group at the University of Leeds. The first draft of the manuscript was written by AGB, with subsequent contributions from all the other coauthors.

Competing interests. The authors declare that they have no conflicts of interest.

490 Financial support. Antonio G. Bruno was funded by a Natural Environment Research Council (NERC) studentship at the University of Leicester, awarded through the Central England NERC Training Alliance (CENTA) (grant no. NE/S007350/1) and by a CASE award from the National Centre for Earth Observation (NCEO). This study was also funded as part of the UK Research and Innovation Natural Environment Research Council's support of the NCEO, grant number NE/R016518/1.





Acknowledgements. The data analysis was performed at the ALICE HPC facility at the University of Leicester. The retrievals were performed on JASMIN, the UK's collaborative data analysis environment (https://www.jasmin.ac.uk) The model simulations were performed on the University of Leeds Advanced Research Computing (ARC) high-performance computing (HPC) machines. We thank Wuhu Feng (NCAS Leeds), Chris Wilson (NCEO Leeds) and Richard Pope (NCEO Leeds) for help with TOMCAT.





#### References

- Akagi, S. K., Yokelson, R. J., Wiedinmyer, C., Alvarado, M. J., Reid, J. S., Karl, T., Crounse, J. D., and Wennberg, P. O.: Emission factors for open and domestic biomass burning for use in atmospheric models, Atmospheric Chemistry and Physics, 11, 4039–4072, https://doi.org/10.5194/acp-11-4039-2011, 2011.
  - Anthony G. Bamston, M. C. and Goldenberg, S. B.: Documentation of a highly ENSO-related sst region in the equatorial pacific: Research note, Atmosphere-Ocean, 35, 367–383, https://doi.org/10.1080/07055900.1997.9649597, 1997.
- Bauer-Marschallinger, B., Paulik, C., Hochstöger, S., Mistelbauer, T., Modanesi, S., Ciabatta, L., Massari, C., Brocca, L., and Wagner, W.: Soil Moisture from Fusion of Scatterometer and SAR: Closing the Scale Gap with Temporal Filtering, Remote Sensing, 10, https://doi.org/10.3390/rs10071030, 2018.
  - Bernath, P. F., Boone, C. D., Steffen, J., and Crouse, J.: Atmospheric Chemistry Experiment SciSat Level 2 Processed Data, v3.5 / v3.6, https://doi.org/10.20383/102.0495, 2021.
- Berrisford, P., Dee, D., Poli, P., Brugge, R., Fielding, M., Fuentes, M., Kållberg, P., Kobayashi, S., Uppala, S., and Simmons, A.: The ERA-Interim archive Version 2.0, Shinfield Park, Reading, 2011.
  - Boone, C., Bernath, P., Cok, D., Jones, S., and Steffen, J.: Version 4 retrievals for the atmospheric chemistry experiment Fourier transform spectrometer (ACE-FTS) and imagers, Journal of Quantitative Spectroscopy and Radiative Transfer, 247, 106 939, https://doi.org/10.1016/j.jqsrt.2020.106939, 2020.
- Bruno, A. G.: Investigating The Trace Gas Emissions Of Biomass Burning In The Earth System, Thesis, University of Leicester, https://doi.org/10.25392/leicester.data.25680108.v1, 2024.
  - Bruno, A. G., Harrison, J. J., Moore, D. P., Chipperfield, M. P., and Pope, R. P.: Satellite observations and modelling of hydrogen cyanide in the Earth's atmosphere, Il Nuovo Cimento C, 6, https://doi.org/10.1393/ncc/i2022-22184-6, 2022.
  - Bruno, A. G., Harrison, J. J., Chipperfield, M. P., Moore, D. P., Pope, R. J., Wilson, C., Mahieu, E., and Notholt, J.: Atmospheric distribution of HCN from satellite observations and 3-D model simulations, Atmospheric Chemistry and Physics, 23, 4849–4861, https://doi.org/10.5194/acp-23-4849-2023, 2023.
  - Bruno, A. G., Moore, D. P., Harrison, J. J., Graham, A., and Chipperfield, M.: Hydrological drivers of hydrogen cyanide wildfire emissions from Indonesian peat fires during the 2015, 2019, and 2023 El Niño events TOMCAT data part 1, https://doi.org/10.5281/ZENODO.17194011, 2025a.
- Bruno, A. G., Moore, D. P., Harrison, J. J., Graham, A., and Chipperfield, M.: Hydrological drivers of hydrogen cyanide wildfire emissions from Indonesian peat fires during the 2015, 2019, and 2023 El Niño events TOMCAT data part 2, https://doi.org/10.5281/ZENODO.17194064, 2025b.
  - Chipperfield, M. P.: New version of the TOMCAT/SLIMCAT off-line chemical transport model: Intercomparison of stratospheric tracer experiments, Quarterly Journal of the Royal Meteorological Society, 132, 1179–1203, https://doi.org/10.1256/qj.05.51, 2006.
- Chipperfield, M. P., Cariolle, D., Simon, P., Ramaroson, R., and Lary, D. J.: A three-dimensional modeling study of trace species in the Arctic lower stratosphere during winter 1989–1990, Journal of Geophysical Research: Atmospheres, 98, 7199–7218, https://doi.org/10.1029/92JD02977, 1993.
  - Chipperfield, M. P., Dhomse, S., Hossaini, R., Feng, W., Santee, M. L., Weber, M., Burrows, J. P., Wild, J. D., Loyola, D., and Coldewey-Egbers, M.: On the Cause of Recent Variations in Lower Stratospheric Ozone, Geophysical Research Letters, 45, 5718–5726, https://doi.org/10.1029/2018GL078071, \_eprint: https://onlinelibrary.wiley.com/doi/pdf/10.1029/2018GL078071, 2018.



540

545

555

570



- 535 Cho, K., Negrón-Juárez, R., Colliander, A., Cosio, E. G., Salinas, N., De Araujo, A., Chambers, J. Q., and Wang, J.: Calibration of the SMAP Soil Moisture Retrieval Algorithm to Reduce Bias Over the Amazon Rainforest, IEEE Journal of Selected Topics in Applied Earth Observations and Remote Sensing, 17, 8724–8736, https://doi.org/10.1109/JSTARS.2024.3388914, 2024.
  - Christian, T. J., Kleiss, B., Yokelson, R. J., Holzinger, R., Crutzen, P., Hao, W. M., Saharjo, B., and Ward, D. E.: Comprehensive laboratory measurements of biomass-burning emissions: 1. Emissions from Indonesian, African, and other fuels, Journal of Geophysical Research: Atmospheres, 108, 2003.
  - Clarisse, L., R'Honi, Y., Coheur, P.-F., Hurtmans, D., and Clerbaux, C.: Thermal infrared nadir observations of 24 atmospheric gases, Geophysical Research Letters, 38, https://doi.org/https://doi.org/10.1029/2011GL047271, 2011.
  - Clerbaux, C., Boynard, A., Clarisse, L., George, M., Hadji-Lazaro, J., Herbin, H., Hurtmans, D., Pommier, M., Razavi, A., Turquety, S., Wespes, C., and Coheur, P.-F.: Monitoring of atmospheric composition using the thermal infrared IASI/MetOp sounder, Atmospheric Chemistry and Physics, 9, 6041–6054, https://doi.org/10.5194/acp-9-6041-2009, 2009.
  - Coheur, P.-F., Clarisse, L., Turquety, S., Hurtmans, D., and Clerbaux, C.: IASI measurements of reactive trace species in biomass burning plumes, Atmospheric Chemistry and Physics, 9, 5655–5667, https://doi.org/10.5194/acp-9-5655-2009, 2009.
  - Dargie, G. C., Lewis, S. L., Lawson, I. T., Mitchard, E. T. A., Page, S. E., Bocko, Y. E., and Ifo, S. A.: Age, extent and carbon storage of the central Congo Basin peatland complex, Nature, 542, 86–90, 2017.
- De Longueville, H., Clarisse, L., Whitburn, S., Franco, B., Bauduin, S., Clerbaux, C., Camy-Peyret, C., and Coheur, P.-F.: Identification of Short and Long-Lived Atmospheric Trace Gases From IASI Space Observations, Geophysical Research Letters, 48, e2020GL091742, https://doi.org/https://doi.org/10.1029/2020GL091742, e2020GL091742 2020GL091742, 2021.
  - Dee, D. P., Uppala, S. M., Simmons, A. J., Berrisford, P., Poli, P., Kobayashi, S., Andrae, U., Balmaseda, M. A., Balsamo, G., Bauer, P., Bechtold, P., Beljaars, A. C. M., van de Berg, L., Bidlot, J., Bormann, N., Delsol, C., Dragani, R., Fuentes, M., Geer, A. J., Haimberger, L., Healy, S. B., Hersbach, H., Hólm, E. V., Isaksen, L., Kållberg, P., Köhler, M., Matricardi, M., McNally, A. P., Monge-Sanz, B. M., Morcrette, J.-J., Park, B.-K., Peubey, C., de Rosnay, P., Tavolato, C., Thépaut, J.-N., and Vitart, F.: The ERA-Interim reanalysis: configuration and performance of the data assimilation system, Quarterly Journal of the Royal Meteorological Society, 137, 553–597,
  - Deeter, M. N.: Calculation and Application of MOPITT Averaging Kernels, https://api.semanticscholar.org/CorpusID:111388701, 2002.
- Duflot, V., Hurtmans, D., Clarisse, L., R'honi, Y., Vigouroux, C., De Mazière, M., Mahieu, E., Servais, C., Clerbaux, C., and Coheur, P.F.: Measurements of hydrogen cyanide (HCN) and acetylene (C<sub>2</sub>H<sub>2</sub>) from the Infrared Atmospheric Sounding Interferometer (IASI),
  Atmospheric Measurement Techniques, 6, 917–925, https://doi.org/10.5194/amt-6-917-2013, 2013.
- Duflot, V., Wespes, C., Clarisse, L., Hurtmans, D., Ngadi, Y., Jones, N., Paton-Walsh, C., Hadji-Lazaro, J., Vigouroux, C., De Mazière, M., Metzger, J.-M., Mahieu, E., Servais, C., Hase, F., Schneider, M., Clerbaux, C., and Coheur, P.-F.: Acetylene (C<sub>2</sub>H<sub>2</sub>) and hydrogen cyanide
   (HCN) from IASI satellite observations: global distributions, validation, and comparison with model, Atmospheric Chemistry and Physics, 15, 10 509–10 527, https://doi.org/10.5194/acp-15-10509-2015, 2015.
  - Entekhabi, D., Yueh, S., and De Lannoy, G.: SMAP handbook, 2014.

https://doi.org/https://doi.org/10.1002/qj.828, 2011.

- Eyring, V., Bony, S., Meehl, G. A., Senior, C. A., Stevens, B., Stouffer, R. J., and Taylor, K. E.: Overview of the Coupled Model Intercomparison Project Phase 6 (CMIP6) experimental design and organization, Geoscientific Model Development, 9, 1937–1958, https://doi.org/10.5194/gmd-9-1937-2016, 2016.
- Fang, B., Lakshmi, V., and Zhang, R.: Validation of downscaled 1-km SMOS and SMAP soil moisture data in 2010–2021, Vadose Zone Journal, 23, e20 305, https://doi.org/10.1002/vzj2.20305, 2024.



575

590

600



- Field, R. D., van der Werf, G. R., Fanin, T., Fetzer, E. J., Fuller, R., Jethva, H., Levy, R., Livesey, N. J., Luo, M., Torres, O., and Worden, H. M.: Indonesian fire activity and smoke pollution in 2015 show persistent nonlinear sensitivity to El Niño-induced drought, Proceedings of the National Academy of Sciences, 113, 9204–9209, https://doi.org/10.1073/pnas.1524888113, 2016.
- Goode, J. G., Yokelson, R. J., Ward, D. E., Susott, R. A., Babbitt, R. E., Davies, M. A., and Hao, W. M.: Measurements of excess O<sub>3</sub>, CO<sub>2</sub>, CO, CH<sub>4</sub>, C<sub>2</sub> H<sub>4</sub>, C<sub>2</sub> H<sub>2</sub>, HCN, NO, NH<sub>3</sub>, HCOOH, CH<sub>3</sub> COOH, HCHO, and CH<sub>3</sub> OH in 1997 Alaskan biomass burning plumes by airborne Fourier transform infrared spectroscopy (AFTIR), Journal of Geophysical Research: Atmospheres, 105, 22 147–22 166, https://doi.org/10.1029/2000JD900287, 2000.
- Graham, A. M., Spracklen, D. V., McQuaid, J. B., Smith, T. E. L., Nurrahmawati, H., Ayona, D., Mulawarman, H., Adam, C., Papargyropoulou, E., Rigby, R., Padfield, R., and Choiruzzad, S.: Updated Smoke Exposure Estimate for Indonesian Peatland Fires Using a Network of Low-Cost PM<sub>2.5</sub> Sensors and a Regional Air Quality Model, GeoHealth, 8, e2024GH001125, https://doi.org/10.1029/2024GH001125, 2024.
- Hayasaka, H., Usup, A., and Naito, D.: New Approach Evaluating Peatland Fires in Indonesian Factors, Remote Sensing, 12, https://doi.org/10.3390/rs12122055, 2020.
  - Hilton, F., Armante, R., August, T., Barnet, C., Bouchard, A., Camy-Peyret, C., Capelle, V., Clarisse, L., Clerbaux, C., Coheur, P.-F., Collard, A., Crevoisier, C., Dufour, G., Edwards, D., Faijan, F., Fourrié, N., Gambacorta, A., Goldberg, M., Guidard, V., Hurtmans, D., Illingworth, S., Jacquinet-Husson, N., Kerzenmacher, T., Klaes, D., Lavanant, L., Masiello, G., Matricardi, M., McNally, A., Newman, S., Pavelin, E., Payan, S., Péquignot, E., Peyridieu, S., Phulpin, T., Remedios, J., Schlüssel, P., Serio, C., Strow, L., Stubenrauch, C., Taylor, J., Tobin, D., Wolf, W., and Zhou, D.: Hyperspectral Earth Observation from IASI: Five Years of Accomplishments, Bulletin of the American Meteorological Society, 93, 347 370, https://doi.org/https://doi.org/10.1175/BAMS-D-11-00027.1, 2012.
  - Hu, Y., Fernandez-Anez, N., Smith, T. E. L., and Rein, G.: Review of emissions from smouldering peat fires and their contribution to regional haze episodes, International Journal of Wildland Fire, 27, 293–312, https://doi.org/10.1071/WF17084, 2018.
- Hu, Y., Christensen, E., Restuccia, F., and Rein, G.: Transient gas and particle emissions from smouldering combustion of peat, Proceedings of the Combustion Institute, 37, 4035–4042, https://doi.org/10.1016/j.proci.2018.06.008, 2019.
  - Huang, B., Thorne, P. W., Banzon, V. F., Boyer, T., Chepurin, G., Lawrimore, J. H., Menne, M. J., Smith, T. M., Vose, R. S., and Zhang, H.-M.: Extended Reconstructed Sea Surface Temperature, Version 5 (ERSSTv5): Upgrades, Validations, and Intercomparisons, Journal of Climate, 30, 8179 8205, https://doi.org/10.1175/JCLI-D-16-0836.1, 2017.
  - Huffman, G., Stocker, E., Bolvin, D., Nelkin, E., and Tan, J.: GPM IMERG Final Precipitation L3 1 day 0.1 degree x 0.1 degree V07, https://doi.org/10.5065/7DE2-M746, artwork Size: 0.000 bytes Pages: 0.000 bytes, 2024.
  - Huijnen, V., Wooster, M. J., Kaiser, J. W., Gaveau, D. L., Flemming, J., Parrington, M., Inness, A., Murdiyarso, D., Main, B., and van Weele, M.: Fire carbon emissions over maritime southeast Asia in 2015 largest since 1997, Scientific reports, 6, 26 886, 2016.
  - Kiely, L., Spracklen, D. V., Wiedinmyer, C., Conibear, L., Reddington, C. L., Archer-Nicholls, S., Lowe, D., Arnold, S. R., Knote, C., Khan, M. F., Latif, M. T., Kuwata, M., Budisulistiorini, S. H., and Syaufina, L.: New estimate of particulate emissions from Indonesian peat fires in 2015, Atmospheric Chemistry and Physics, 19, 11 105–11 121, https://doi.org/10.5194/acp-19-11105-2019, 2019.
  - Kleinböhl, A., Toon, G. C., Sen, B., Blavier, J.-F. L., Weisenstein, D. K., Strekowski, R. S., Nicovich, J. M., Wine, P. H., and Wennberg, P. O.: On the stratospheric chemistry of hydrogen cyanide, Geophysical Research Letters, 33, https://doi.org/10.1029/2006GL026015, 2006.
  - Li, Q., Jacob, D. J., Bey, I., Yantosca, R. M., Zhao, Y., Kondo, Y., and Notholt, J.: Atmospheric hydrogen cyanide (HCN): Biomass burning source, ocean sink?, Geophysical Research Letters, 27, 357–360, https://doi.org/10.1029/1999GL010935, 2000.



615



- 610 Ma, H., Zeng, J., Zhang, X., Peng, J., Li, X., Fu, P., Cosh, M. H., Letu, H., Wang, S., Chen, N., and Wigneron, J.-P.: Surface soil moisture from combined active and passive microwave observations: Integrating ASCAT and SMAP observations based on machine learning approaches, Remote Sensing of Environment, 308, 114 197, https://doi.org/10.1016/j.rse.2024.114197, 2024.
  - Monks, S. A., Arnold, S. R., Hollaway, M. J., Pope, R. J., Wilson, C., Feng, W., Emmerson, K. M., Kerridge, B. J., Latter, B. L., Miles, G. M., Siddans, R., and Chipperfield, M. P.: The TOMCAT global chemical transport model v1.6: description of chemical mechanism and model evaluation, Geoscientific Model Development, 10, 3025–3057, https://doi.org/10.5194/gmd-10-3025-2017, 2017.
  - Moore, D. P., Bruno, A. G., Harrison, J. J., and Remedios, J.: CO and HCN retrievals from IASI measurements: validation and global scale variability, in Preparation.
  - Morgenstern, O., Hegglin, M. I., Rozanov, E., O'Connor, F. M., Abraham, N. L., Akiyoshi, H., Archibald, A. T., Bekki, S., Butchart, N., Chipperfield, M. P., Deushi, M., Dhomse, S. S., Garcia, R. R., Hardiman, S. C., Horowitz, L. W., Jöckel, P., Josse, B., Kinnison, D.,
- Lin, M., Mancini, E., Manyin, M. E., Marchand, M., Marécal, V., Michou, M., Oman, L. D., Pitari, G., Plummer, D. A., Revell, L. E., Saint-Martin, D., Schofield, R., Stenke, A., Stone, K., Sudo, K., Tanaka, T. Y., Tilmes, S., Yamashita, Y., Yoshida, K., and Zeng, G.: Review of the global models used within phase 1 of the Chemistry–Climate Model Initiative (CCMI), Geoscientific Model Development, 10, 639–671, https://doi.org/10.5194/gmd-10-639-2017, 2017.
- Nayak, A. K., Xu, X., Frey, S. K., Khader, O., Erler, A. R., Lapen, D. R., Russell, H. A. J., and Sudicky, E. A.: Quantifying the potential of using Soil Moisture Active Passive (SMAP) soil moisture variability to predict subsurface water dynamics, Hydrology and Earth System Sciences, 29, 215–244, https://doi.org/10.5194/hess-29-215-2025, 2025.
  - Nechita-Banda, N., Krol, M., van der Werf, G. R., Kaiser, J. W., Pandey, S., Huijnen, V., Clerbaux, C., Coheur, P., Deeter, M. N., and Röckmann, T.: Monitoring emissions from the 2015 Indonesian fires using CO satellite data, Philosophical Transactions of the Royal Society B: Biological Sciences, 373, 20170 307, https://doi.org/10.1098/rstb.2017.0307, 2018.
- Nurdiati, S., Sopaheluwakan, A., and Septiawan, P.: Spatial and Temporal Analysis of El Niño Impact on Land and Forest Fire in Kalimantan and Sumatra, Agromet, 35, 1–10, https://doi.org/10.29244/j.agromet.35.1.1-10, 2021.
  - ONeill, P., Chan, S., Njoku, E., Jackson, T., Bindlish, R., and Chaubell, J.: SMAP L3 Radiometer Global Daily 36 km EASE-Grid Soil Moisture, Version 8, https://doi.org/10.5067/OMHVSRGFX38O, 2021.
- Page, S. E. and Hooijer, A.: In the line of fire: the peatlands of Southeast Asia, Philosophical Transactions of the Royal Society B: Biological Sciences, 371, 20150 176, https://doi.org/10.1098/rstb.2015.0176, 2016.
  - Park, M., Worden, H. M., Kinnison, D. E., Gaubert, B., Tilmes, S., Emmons, L. K., Santee, M. L., Froidevaux, L., and Boone, C. D.: Fate of Pollution Emitted During the 2015 Indonesian Fire Season, Journal of Geophysical Research: Atmospheres, 126, e2020JD033474, https://doi.org/10.1029/2020JD033474, e2020JD033474 2020JD033474, 2021.
- Parker, R. J., Boesch, H., Wooster, M. J., Moore, D. P., Webb, A. J., Gaveau, D., and Murdiyarso, D.: Atmospheric CH<sub>4</sub> and CO<sub>2</sub> enhancements and biomass burning emission ratios derived from satellite observations of the 2015 Indonesian fire plumes, Atmospheric Chemistry and Physics, 16, 10111–10131, https://doi.org/10.5194/acp-16-10111-2016, 2016.
  - Pope, R. J., Arnold, S. R., Chipperfield, M. P., Reddington, C. L. S., Butt, E. W., Keslake, T. D., Feng, W., Latter, B. G., Kerridge, B. J., Siddans, R., Rizzo, L., Artaxo, P., Sadiq, M., and Tai, A. P. K.: Substantial Increases in Eastern Amazon and Cerrado Biomass Burning-Sourced Tropospheric Ozone, Geophysical Research Letters, 47, e2019GL084143, https://doi.org/10.1029/2019GL084143, \_eprint: https://onlinelibrary.wiley.com/doi/pdf/10.1029/2019GL084143, 2020.



665

675



- Pradhan, R. K., Markonis, Y., Vargas Godoy, M. R., Villalba-Pradas, A., Andreadis, K. M., Nikolopoulos, E. I., Papalexiou, S. M., Rahim, A., Tapiador, F. J., and Hanel, M.: Review of GPM IMERG performance: A global perspective, Remote Sensing of Environment, 268, 112 754, https://doi.org/https://doi.org/10.1016/j.rse.2021.112754, 2022.
- Pumphrey, H. C., Glatthor, N., Bernath, P. F., Boone, C. D., Hannigan, J. W., Ortega, I., Livesey, N. J., and Read, W. G.: MLS measurements of stratospheric hydrogen cyanide during the 2015–2016 El Niño event, Atmospheric Chemistry and Physics, 18, 691–703, https://doi.org/10.5194/acp-18-691-2018, 2018.
  - Randerson, J., Van Der Werf, G., Giglio, L., Collatz, G., and Kasibhatla, P.: Global Fire Emissions Database, Version 4.1 (GFEDv4), https://doi.org/10.3334/ORNLDAAC/1293, 2017.
  - Rodgers, G. J.: Optimal Estimation, Springer, New York, NY, 2000.
- Rodriguez Vasquez, M. J., Benoist, A., Roda, J.-M., and Fortin, M.: Estimating greenhouse gas emissions from peat combustion in wildfires on Indonesian peatlands, and their uncertainty, Global Biogeochemical Cycles, 35, e2019GB006218, 2021.
  - Rosanka, S., Franco, B., Clarisse, L., Coheur, P.-F., Pozzer, A., Wahner, A., and Taraborrelli, D.: The impact of organic pollutants from Indonesian peatland fires on the tropospheric and lower stratospheric composition, Atmospheric Chemistry and Physics, 21, 11257–11288, https://doi.org/10.5194/acp-21-11257-2021, 2021.
- 660 Santoso, A., Mcphaden, M. J., and Cai, W.: The Defining Characteristics of ENSO Extremes and the Strong 2015/2016 El Niño, Reviews of Geophysics, 55, 1079–1129, https://doi.org/10.1002/2017RG000560, 2017.
  - Schroeder, W., Oliva, P., Giglio, L., and Csiszar, I. A.: The New VIIRS 375m active fire detection data product: Algorithm description and initial assessment, Remote Sensing of Environment, 143, 85–96, https://doi.org/https://doi.org/10.1016/j.rse.2013.12.008, 2014.
  - Sheese, P. E., Walker, K. A., and Boone, C. D.: A global enhancement of hydrogen cyanide in the lower stratosphere throughout 2016, Geophysical Research Letters, 44, 5791–5797, https://doi.org/https://doi.org/10.1002/2017GL073519, 2017.
  - Singh, H. B., Brune, W. H., Crawford, J. H., Flocke, F., and Jacob, D. J.: Chemistry and transport of pollution over the Gulf of Mexico and the Pacific: spring 2006 INTEX-B campaign overview and first results, Atmospheric Chemistry and Physics, 9, 2301–2318, https://doi.org/10.5194/acp-9-2301-2009, 2009.
- Stockwell, C., Yokelson, R., Kreidenweis, S., Robinson, A., DeMott, P., Sullivan, R., Reardon, J., Ryan, K., Griffith, D., and Stevens,

  L.: Trace gas emissions from combustion of peat, crop residue, domestic biofuels, grasses, and other fuels: configuration and Fourier transform infrared (FTIR) component of the fourth Fire Lab at Missoula Experiment (FLAME-4), Atmospheric chemistry and physics,

  14, 9727–9754, 2014.
  - Stockwell, C. E., Jayarathne, T., Cochrane, M. A., Ryan, K. C., Putra, E. I., Saharjo, B. H., Nurhayati, A. D., Albar, I., Blake, D. R., Simpson, I. J., et al.: Field measurements of trace gases and aerosols emitted by peat fires in Central Kalimantan, Indonesia, during the 2015 El Niño, Atmospheric Chemistry and Physics, 16, 11711–11732, 2016.
  - Usup, A., Hashimoto, Y., Takahashi, H., and Hayasaka, H.: Combustion and thermal characteristics of peat fire in tropical peatland in Central Kalimantan, Indonesia, Tropics, 14, 1–19, https://doi.org/10.3759/tropics.14.1, 2004.
  - van der Werf, G. R., Randerson, J. T., Giglio, L., van Leeuwen, T. T., Chen, Y., Rogers, B. M., Mu, M., van Marle, M. J. E., Morton, D. C., Collatz, G. J., Yokelson, R. J., and Kasibhatla, P. S.: Global fire emissions estimates during 1997–2016, Earth System Science Data, 9, 697–720, https://doi.org/10.5194/essd-9-697-2017, 2017.
  - Vetrita, Y. and Cochrane, M. A.: Fire Frequency and Related Land-Use and Land-Cover Changes in Indonesia's Peatlands, Remote Sensing, 12, https://doi.org/10.3390/rs12010005, 2020.





- Whitburn, S., Van Damme, M., Clarisse, L., Hurtmans, D., Clerbaux, C., and Coheur, P.-F.: IASI-derived NH<sub>3</sub> enhancement ratios relative to CO for the tropical biomass burning regions, Atmospheric Chemistry and Physics, 17, 12 239–12 252, https://doi.org/10.5194/acp-17-12239-2017, 2017.
- Wiedinmyer, C., Akagi, S. K., Yokelson, R. J., Emmons, L. K., Al-Saadi, J. A., Orlando, J. J., and Soja, A. J.: The Fire INventory from NCAR (FINN): a high resolution global model to estimate the emissions from open burning, Geoscientific Model Development, 4, 625–641, https://doi.org/10.5194/gmd-4-625-2011, 2011.
- Yokelson, R. J., Saharjo, B. H., Stockwell, C. E., Putra, E. I., Jayarathne, T., Akbar, A., Albar, I., Blake, D. R., Graham, L. L., Kurniawan,
   A., et al.: Tropical peat fire emissions: 2019 field measurements in Sumatra and Borneo and synthesis with previous studies, Atmospheric chemistry and physics, 22, 10 173–10 194, 2022.
  - Zhang, T., Wooster, M. J., and Xu, W.: Approaches for synergistically exploiting VIIRS I- and M-Band data in regional active fire detection and FRP assessment: A demonstration with respect to agricultural residue burning in Eastern China, Remote Sensing of Environment, 198, 407–424, https://doi.org/https://doi.org/10.1016/j.rse.2017.06.028, 2017.